Weyl, Dirac and high-fold chiral fermions in topological quantum matter

M. Zahid Hasan[1,2,3,4]✉, *Guoqing Chang*[1,5]✉, *Ilya Belopolski*[1], *Guang Bian*[1,6], *Su-Yang Xu*[1,7] *and Jia-Xin Yin*[1]

Abstract | Quantum materials hosting Weyl fermions have opened a new era of research in condensed matter physics. First proposed in 1929 in the context of particle physics, Weyl fermions have yet to be observed as elementary particles. In 2015, Weyl fermions were detected as collective electronic excitations in the strong spin–orbit coupled material tantalum arsenide, TaAs. This discovery was followed by a flurry of experimental and theoretical explorations of Weyl phenomena in materials. Weyl materials naturally lend themselves to the exploration of the topological index associated with Weyl fermions and their divergent Berry curvature field, as well as the topological bulk–boundary correspondence, giving rise to protected conducting surface states. Here, we review the broader class of Weyl topological phenomena in materials, starting with the observation of emergent Weyl fermions in the bulk and Fermi arc states on the surface of the TaAs family of crystals by photoemission spectroscopy. We then discuss several exotic optical and magnetic responses observed in these materials, as well as progress in developing related chiral materials. We discuss the conceptual development of high-fold chiral fermions, which generalize Weyl fermions, and we review the observation of high-fold chiral fermion phases by taking the rhodium silicide, RhSi, family of crystals as a prime example. Lastly, we discuss recent advances in Weyl line phases in magnetic topological materials. With this Review, we aim to provide an introduction to the basic concepts underlying Weyl physics in condensed matter, and to representative materials and their electronic structures and topology as revealed by spectroscopic studies. We hope this work serves as a guide for future theoretical and experimental explorations of chiral fermions and related topological quantum systems with potentially enhanced functionalities.

The cross-pollination between high-energy and condensed matter physics has led to a more profound understanding of the fundamental organizing principles of matter, leading to concepts such as spontaneous symmetry breaking, phase transitions and renormalization[1–3]. Such knowledge has, in turn, greatly helped researchers understand the inner workings of magnets, superconductors and other exotic states of matter[4–13]. The observation of massless Dirac fermions in graphene and topological insulators has become a cornerstone of the past decade's research activity in condensed matter[5–7,10,11]. In the past few years, Weyl semimetals and related Dirac and high-fold fermion materials have emerged as the new frontier along this line of research[8,9,14–35]. Weyl fermions, a subset of Dirac fermions, were first introduced in 1929 in the context of high-energy physics as massless particles with definite chirality, described by a two-component spinor obeying the Weyl equation. Despite their long history, Weyl fermions have yet to be observed as fundamental particles. The realization of emergent Weyl fermions in quantum materials not only provides the first example of Weyl fermions in nature but makes it possible to access a kaleidoscope of novel quantum phenomena in tunable systems[8,9,21–32]. Inspired by the richness of electronic structures in quantum matter, Weyl fermions were generalized to describe topological fermions beyond the two-component Weyl fermions considered in high-energy physics[36,37].

Such generalized topological fermions form a catalogue of 0D point degeneracies of bands in momentum space. These fermions can be classified by their topological invariants (BOX 1), the dimensionality of momentum

✉e-mail: *mzhasan@princeton.edu*; *guoqing.chang@ntu.edu.sg*

https://doi.org/10.1038/s41578-021-00301-3

space in which they arise and the number of bands that cross to form the point degeneracy. These unconventional fermions include higher-fold (three-fold, four-fold and six-fold) chiral fermions in 3D crystals[38–50]. They are characterized by a Chern number topological invariant, also called the chiral charge[8,9]. The topological invariants associated with chiral fermions guarantee the existence of protected boundary modes, the Fermi arcs, which are open surface states on the terminated surface of the material[33]. Recent theories found that all point-like degeneracies in non-magnetic, structurally chiral crystals with spin–orbit coupling (SOC) are chiral-charged fermions[40]. By contrast, most high-fold degenerate fermions in structurally achiral space groups do not possess chiral charges, such as four-fold Dirac fermions[51–54] and eight-fold double Dirac fermions[39,55]. Another catalogue of topological band structures consists of nodal lines, where bands are degenerate along an entire closed curve in momentum space. Such 1D band crossings exhibit a winding number topological invariant that protects topological drumhead surface states[56–69] (BOX 1). Unlike point degeneracies, nodal lines can exhibit rich composite structures, including nodal chains, Hopf links and nodal knots[70–77]. A third catalogue consists of hybrid 0D and 1D degeneracies, where three-fold point degeneracies serve as boundary points interconnecting two-fold nodal lines[78–83].

Topological fermions often give rise to anomalous electronic, magnetic and optical responses, especially in cases where the topology is associated with momentum-space singularities of the Berry curvature field[8,9,21–27] (BOX 1). For example, topological fermions can support unconventional superconductivity[84–88] or a large anomalous Hall effect in topological magnets[89]. Under an external magnetic field, Weyl fermions can realize the chiral anomaly[90–93], the chiral magnetic effect[94–96], the quantum nonlinear Hall effect[97] and nonlocal transport[98,99]. The magnetic orbits arising from open Fermi arc surface states and bulk chiral Landau levels can induce unusual quantum oscillations[100–103]. Weyl semimetals can also support exotic nonlinear optical responses, which may be useful for new solar cells or light sensors[104–113]. The rich quantum properties of Weyl semimetals have been argued to have potential applications in next-generation quantum devices[8,9,21–32].

The goal of this Review is to survey the research progress in this field with a focus on electronic structure as revealed by photoemission spectroscopy. Several excellent reviews have summarized the large body of developments reported between 2015 and 2018 (REFS[21–27]), thus, here, after reviewing the basics, we mostly emphasize the latest progress and the new frontiers. Although the focus of this Review is on spectroscopic experiments and materials development, we do include some basic theory in order to provide an overall conceptual scenario and experimental understanding of the materials. The first section provides the basic theoretical background, emphasizing the topological aspects. The second section reviews the experimental observation of the Weyl semimetal phase[28,29], focusing on spectroscopic observations based on angle-resolved photoemission spectroscopy (ARPES)[28,29,114–125], and summarizes experiments that reported unusual magnetic and optical responses in the tantalum arsenide, TaAs, family of materials[109,110,126–133]. The third section highlights the experimental progress in type-II Weyl fermion and related metals[36,37,134–154]. The fourth section introduces topological chiral crystals as generalized versions of Weyl semimetals[40], highlighting the recent observation of giant helicoid Fermi arcs in the rhodium silicide, RhSi, family of materials[41–46]. The fifth section focuses on the Weyl line phase with drumhead surface states observed in magnetic materials[56–77]. Finally, in the outlook, we identify promising new research directions, such as the exploration of tunable topological magnets.

Weyl fermions in condensed matter physics

Weyl fermions arise as low-energy quasiparticle excitations in 3D crystals lacking inversion symmetry or time-reversal symmetry or both[8,9,21–32]. In a Weyl semimetal, Weyl fermions are the sources and sinks of the Berry curvature field in momentum space[8,9,15–35] (BOX 1 and lower part of FIG. 1a). The integral of the Berry curvature field of any 2D manifold enclosing a Weyl node is a quantized integer, which defines the Chern number, or chiral charge, of the Weyl fermion[33]. FIGURE 1a shows a schematic of two oppositely charged (chiral) Weyl fermions in the bulk[33]. A plane cutting between the Weyl fermions exhibits a Chern number $|C| = 1$, whose Hamiltonian, $H_y(k_x, k_z)$, represents a 2D Chern insulator with a 1D chiral edge mode (FIG. 1b). Such a chiral edge state can be obtained on any plane between the two Weyl points. In this way, a topologically protected 2D open surface state, the Fermi arc, is formed between two oppositely charged Weyl fermions (FIG. 1c). The isoenergetic contour of a Fermi arc is an open Fermi surface connecting projected Weyl pockets (top part of FIG. 1a). This is different from a conventional 2D electron dispersion, whose Fermi surface is a closed contour. What is more, Fermi arc surface states can take helicoidal structures described by non-compact Riemann surfaces[43,155,156].

Weyl fermions are local singularities in energy and momentum, so their exotic response arises only in a finite, topologically non-trivial energy and momentum window. In a simple picture, Weyl fermions can be viewed as arising from a band inversion, in which the conduction band sinks below the valence band in energy[30–35] (FIG. 1d). In this picture, the topologically non-trivial window is closely related to the degree of band inversion, which determines the momentum-space separation of the Weyl fermions and their extent

Author addresses

[1]Laboratory for Topological Quantum Matter and Advanced Spectroscopy (B7), Department of Physics, Princeton University, Princeton, NJ, USA.
[2]Materials Sciences Division, Lawrence Berkeley National Laboratory, Berkeley, CA, USA.
[3]Princeton Institute for the Science and Technology of Materials, Princeton University, Princeton, NJ, USA.
[4]Quantum Science Center, Oak Ridge, TN, USA.
[5]Division of Physics and Applied Physics, School of Physical and Mathematical Sciences, Nanyang Technological University, Singapore, Singapore.
[6]Department of Physics and Astronomy, University of Missouri, Columbia, MO, USA.
[7]Department of Chemistry and Chemical Biology, Harvard University, Cambridge, MA, USA.

Box 1 | **Topological invariants and Weyl fermions**

Topological invariants are integer indices that define the topology and determine the exotic properties of topological quantum materials[5–7,10,11]. These quantized invariants are rooted in the Berry phase γ_m (REF.[202]), which is acquired by a path integral in momentum space from the Bloch wave functions $|m(\mathbf{k})\rangle$ over evolution of the Hamiltonian $\mathcal{H}(\mathbf{k})$:

$$\gamma_m = \int_c \mathcal{A}_m(\mathbf{k}) \cdot \mathrm{d}\mathbf{k}, \quad (1)$$

where $\mathcal{A}_m(\mathbf{k})$ is a vector-valued function called the Berry connection:

$$\mathcal{A}_m(\mathbf{k}) = i\left\langle m(\mathbf{k}) \left| \frac{\partial}{\partial \mathbf{k}} \right| m(\mathbf{k}) \right\rangle. \quad (2)$$

The integrated Berry connection along any path encircling a topological nodal line is a quantized integer $\gamma = \pi$ (panel **a** of the figure, where the big black circle represents the nodal line in momentum space and the coloured dashed lines show two different paths encircling it). The quantized Berry phase of a nodal line is the same as the winding number for gapless points in 2D systems, such as the massless Dirac fermions in graphene[5].

The topological invariant of 3D Weyl fermions is associated with the Berry curvature field:

$$\mathbf{\Omega}_m(\mathbf{k}) = \nabla_{\mathbf{k}} \times \mathcal{A}_m(\mathbf{k}). \quad (3)$$

Weyl fermions behave as sources or sinks of the Berry curvature field (panel **b** of the figure). The integral of the Berry curvature field (black arrows) of any 2D manifold (such as the red and blue spheres in the figure) enclosing a Weyl point is an integer, the Chern number or chiral charge of the Weyl point:

$$C_m = \frac{1}{2\pi} \int_S \mathbf{\Omega}_m(\mathbf{k}) \mathrm{d}\mathbf{S}. \quad (4)$$

The Berry curvature field has the same transformation properties as a magnetic field under inversion and time-reversal symmetry. In this sense, the Berry curvature field can be viewed as the magnetic field in momentum space. Therefore, Weyl fermions can be interpreted as magnetic monopoles in momentum space. Due to the quantized chiral charge of each Weyl node, making two oppositely charged Weyl fermions meet in momentum space is the only way to annihilate Weyl fermions in a periodic system.

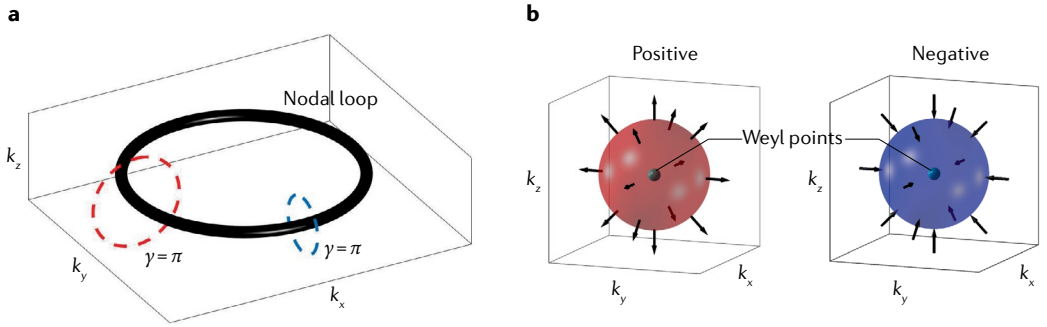

in energy[26,119,135,146]. For a given energy within the topological window, the electronic structure exhibits pockets associated with a non-zero chiral charge (FIG. 1e, top). However, if one sweeps in energy out of the topological window, pockets with opposite chiral charge merge and are then associated with zero chiral charge (FIG. 1e, bottom). Considering the surface states, within the topological energy window, topological Fermi arcs connect bulk pockets with opposite chiral charge. Outside of the topological energy window, no Fermi arc is topologically protected, although studies do report that a non-topological arc may persist, depending on details of the electronic structure of the specific material, the crystalline surface termination and other parameters (dashed line in FIG. 1e). The topologically non-trivial window is an important consideration when exploring optical, magnetic or other responses of a material hosting Weyl fermions[26,119,135,146]. For example, for many applications, it is crucial that the Fermi level sits within the topological window or that optical transitions occur within the topological window. The advent of Kramers–Weyl fermions in structurally chiral crystals, discussed in the section on topological chiral crystals, marked an important development in the search for materials with larger topological windows. Chiral crystals naturally give rise to Weyl fermions pinned to Kramers points in the bulk Brillouin zone, producing Weyl fermions with maximal separation in momentum space[40] (FIG. 1f). Such systems can produce topological energy windows substantially larger than those found in achiral Weyl semimetals.

In the simplest case, a Weyl fermion is a two-fold degenerate band crossing of two singly degenerate bands with linear dispersion in all three momentum-space directions (FIG. 1g). Because crystalline quasiparticles need not respect Lorentz invariance, Weyl fermions in condensed matter can exhibit a wider variety of dispersions and exotic properties than relativistic Weyl fermions. This is well illustrated by the case of type-II Weyl fermions[36,37] (FIG. 1h). The difference between type-I and

type-II Weyl fermions lies in the degree of Weyl cone tilt. The two bands of type-I Weyl fermions can be slightly tilted, but they keep opposite signs of Fermi velocities in all directions. By contrast, the bands forming type-II Weyl fermions are strongly tilted in at least one direction, where their Fermi velocities have the same sign[36,37].

Under additional crystal symmetries, Weyl fermions can have other types of electronic structures, rather than

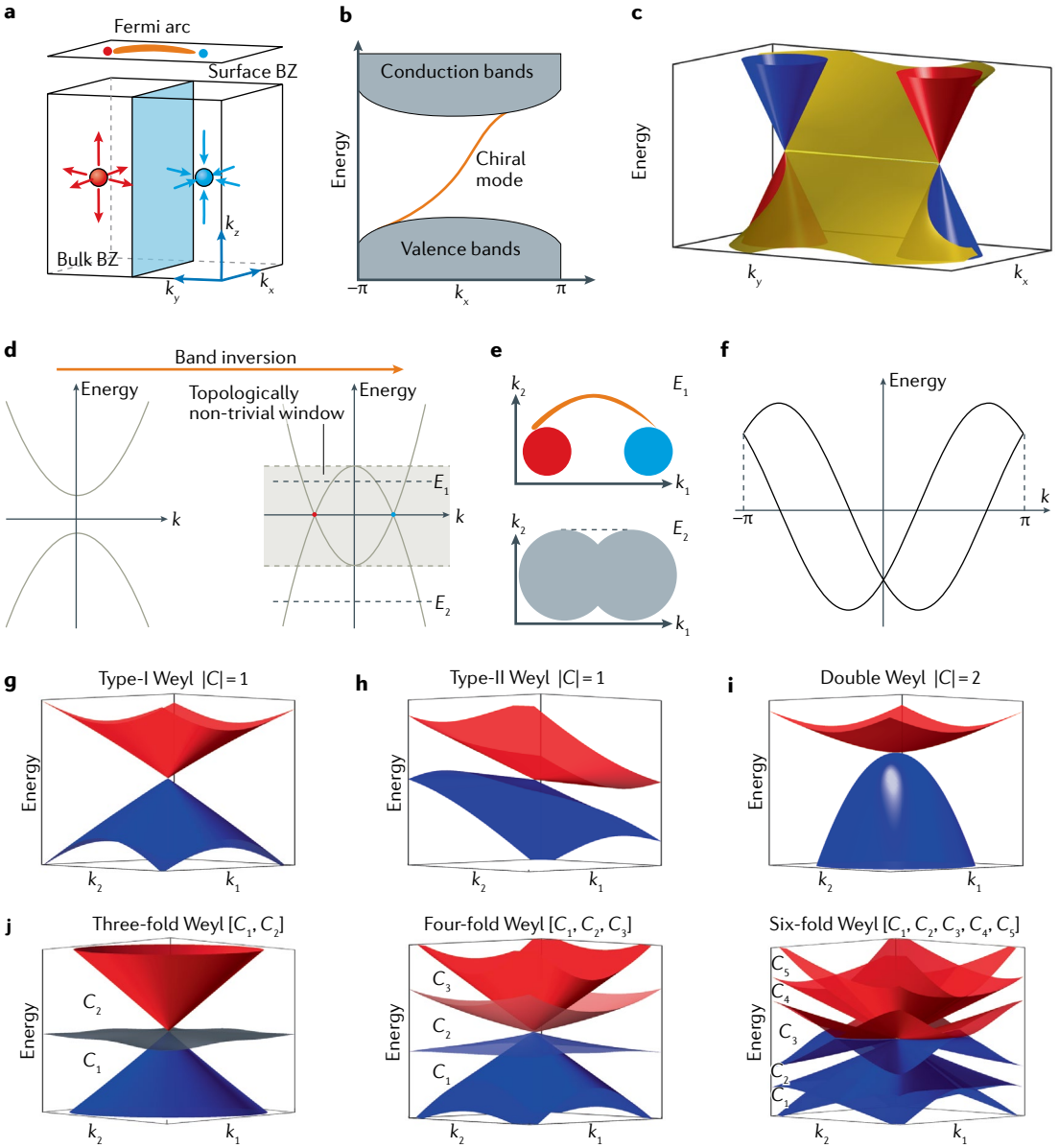

Fig. 1 | **Topology and classification of Weyl fermions. a** | Schematic illustration of two Weyl fermions in the bulk Brillouin zone (BZ) and of the Fermi arc (orange) in the surface BZ. The red and blue spheres represent Weyl fermions with opposite chiral charge. The arrows illustrate the direction of the Berry curvature field in the vicinity of each Weyl fermion. **b** | The blue plane in panel **a** in between two Weyl fermions illustrates a 2D subsystem carrying Chern number $C = 1$, which induces a chiral edge mode connecting the conduction and valence bands on the 1D edge of the 2D subsystem. **c** | Schematic illustration of the Fermi arc surface state (yellow surface) between two oppositely charged Weyl fermions (red cones: $C = +1$, blue cones: $C = -1$) in energy–momentum space. **d** | Weyl fermions can be generated via band inversion in crystals breaking time-reversal or inversion symmetry. The two-fold band crossings form two Weyl fermions with opposite chiral charge. The topologically non-trivial energy window lies between the band extrema (dashed gray lines). **e** | Bulk pockets and surface states at different energies in a Weyl semimetal. Top: within the topologically non-trivial energy window (for example, at the energy E_1 marked in panel **d**), bulk pockets of opposite chiral charge are isolated. A topological Fermi arc (orange line) connects projected bulk pockets in the surface BZ. Bottom: outside the topologically non-trivial energy window (for example, at the energy E_2 marked in panel **d**), the two Weyl fermions merge into one trivial (grey) pocket. No topological Fermi arc is protected. **f** | Kramers–Weyl fermions in non-magnetic chiral crystals arise due to spin–orbit coupling, without band inversion. **g–i** | Classification of different two-fold Weyl fermions by their E–k dispersions and topological chiral charges. **j** | Energy dispersions of high-fold chiral fermions. The topological invariants of an n-fold chiral fermion can be defined by the Chern numbers of each band (red bands: $C > 0$, blue bands: $C < 0$, grey band: $C = 0$) or, equivalently, by the Chern numbers of the $n - 1$ band gaps.

the conventional two-fold degenerate linear dispersions. For example, four-fold or six-fold rotation axes allow double Weyl fermions with charge $|C| = 2$. Six-fold rotation axes allow triple Weyl fermions with charge $|C| = 3$ (REF.[157]). The energy dispersion of a double and triple Weyl fermion is still linear along the rotation axis but is quadratic and cubic, respectively, in the plane normal to the axis (FIG. 1i). A double Weyl fermion can be viewed as two singly charged Weyl fermions stuck together in momentum space, which become three for a triple Weyl fermion. If the high-fold rotation symmetry is broken, a double Weyl fermion splits into two, and a triple Weyl fermion into three, conventional singly charged Weyl fermions[157–159].

In non-magnetic 3D crystals, apart from two-fold degenerate Weyl fermions, point fermions with three-fold, four-fold, six-fold and eight-fold degeneracy are allowed[38–50,55,78–83]. These high-fold fermions can be classified into two groups: chiral fermions and non-chiral fermions. High-fold chiral fermions are natural generalizations of two-fold Weyl fermions[38–42]. There are two approaches to classify the topology of n-fold chiral fermions. One way is to determine the Chern number of each band[39] and the other is to calculate the chiral charges for the $n-1$ band gaps $[C_1, C_2,..., C_{n-1}]$ (REF.[41]) (FIG. 1j). High-fold non-chiral fermions have no well-defined chiral charge[55,78–83]. In most cases, one can not determine whether an n-fold fermion is chiral or not simply from the point node degeneracy. High-fold degenerate fermions display complex space groups dependent on band dispersions and topology. For example, the three-fold fermions at the P-point in the space group no. 199 are the spin-1 generalization of Weyl fermions[39], whereas the three-fold fermions in the space group no. 220 and the three-fold linking points in the space groups nos. 156–159 and nos. 187–190 do not have quantized chiral charges[78–83]. Four-fold Dirac fermions in centrosymmetric crystals are non-chiral[26], whereas four-fold fermions at the Γ point of cubic chiral crystals have quantized chiral charges[40–42]. It is worth noting that all point degeneracies in non-magnetic chiral crystals are chiral fermions with quantized non-zero Chern numbers[40]. This universal topological electronic property of non-magnetic chiral crystals provides a powerful tool for searching for new topological chiral materials.

First Weyl semimetals: the TaAs family

The material realization of Weyl topology was inspired by the development of topological insulators. The first materials prediction was in the pyrochlore iridates family, $R_2Ir_2O_7$ (R is a rare-earth element) in 2011 (REF.[33]). To realize Weyl fermions, the authors of this work argued for a special kind of anti-ferromagnetic order with an all-in/all-out configuration to break time-reversal symmetry in $R_2Ir_2O_7$ (REF.[33]). However, ARPES measurements on these materials have not been reported. Moreover, the assumed magnetic order is still under debate in experiments[160,161]. Another work proposed to realize Weyl fermions in a superlattice consisting of a stack of alternating thin films of a topological insulator and a normal ferromagnetic insulator[34,162]. No experiment has been reported, possibly owing to the lack of a suitable ferromagnetic insulator with a lattice matching that of known topological insulators. The next proposal that was put forward suggested $HgCr_2Se_4$ (REF.[158]), which is known to be a natural ferromagnet with a fairly high Curie temperature of ≃120 K (REF.[163]). However, ARPES experiments have not been successful on this compound.

The TaAs materials family. The breakthrough finally took place in early 2015, when the first Weyl fermion material was predicted and experimentally observed in the inversion-symmetry-breaking TaAs family of crystals[28–31]. The TaAs family has a body-centred tetragonal lattice system in space group $I4_1md$, no. 109. The crystal consists of interpenetrating Ta/Nb and As/P sublattices (FIG. 2a). The lattice lacks inversion symmetry, which is the key condition for realizing Weyl fermions. According to density functional theory (DFT) calculations, there are two groups of Weyl fermions near the Fermi level in TaAs and its cousins. One group of Weyl fermions, W_1, lies at $k_z = 2\pi/c$ (cyan plane in FIG. 2b), whereas the other group, W_2, lies closer to Γ (REFS[30,31]). The W_2 Weyl fermions and their Fermi arc surface states have been directly observed by ARPES[28,29,116]. FIGURE 2c shows the Fermi surface obtained by soft X-ray (SX)-ARPES, which selectively enhances the states from the bulk at the Fermi level by using a high incident photon energy[28]. On this constant-energy cut, ARPES shows pairs of point-like Fermi surfaces (indicated by the arrows in FIG. 2c). The k-space locations and separations of the bulk Fermi points are consistent with the location of W_2 Weyl fermions in DFT calculations[28,29,116]. Moreover, the bands disperse linearly away from the gapless nodes, as expected for Weyl fermions (FIG. 2d). To provide further evidence for the presence of Weyl fermions, the experimental observation of Fermi arc surface states was needed. On the (001) surface, two W_2 Weyl fermions of the same chiral charge project at the same k-point. According to the topological bulk–boundary correspondence, there should, therefore, be two Fermi arc surface states originating from one k-point on the surface. Indeed, on the surface, ultraviolet (UV)-ARPES revealed crescent-shaped surface states, which correspond to the theoretical predictions for Fermi arcs (FIG. 2e). When the bulk nodes measured by SX-ARPES are superimposed onto the Fermi surfaces measured by low-photon-energy UV-ARPES, the surface Fermi arc terminations match with the projections of the bulk Weyl fermions on the surface Brillouin zone[28] (FIG. 2f,g). The bulk and surface evidence, taken together, confirms the presence of Weyl fermions in TaAs. Similar surface states were observed in the other materials of the TaAs family: NbAs, TaP and NbP (REFS[114–120]). A large spin polarization of the Fermi arcs, approaching 80%, was observed in TaAs, consistent with theoretical predictions[121,122]. Scanning tunnelling microscopy (STM) measurements, through quasiparticle interference, also showed signatures of Fermi arcs in the TaAs family[123–125]. These complementary spectroscopy measurements by different groups of different compounds thus provided further evidence for

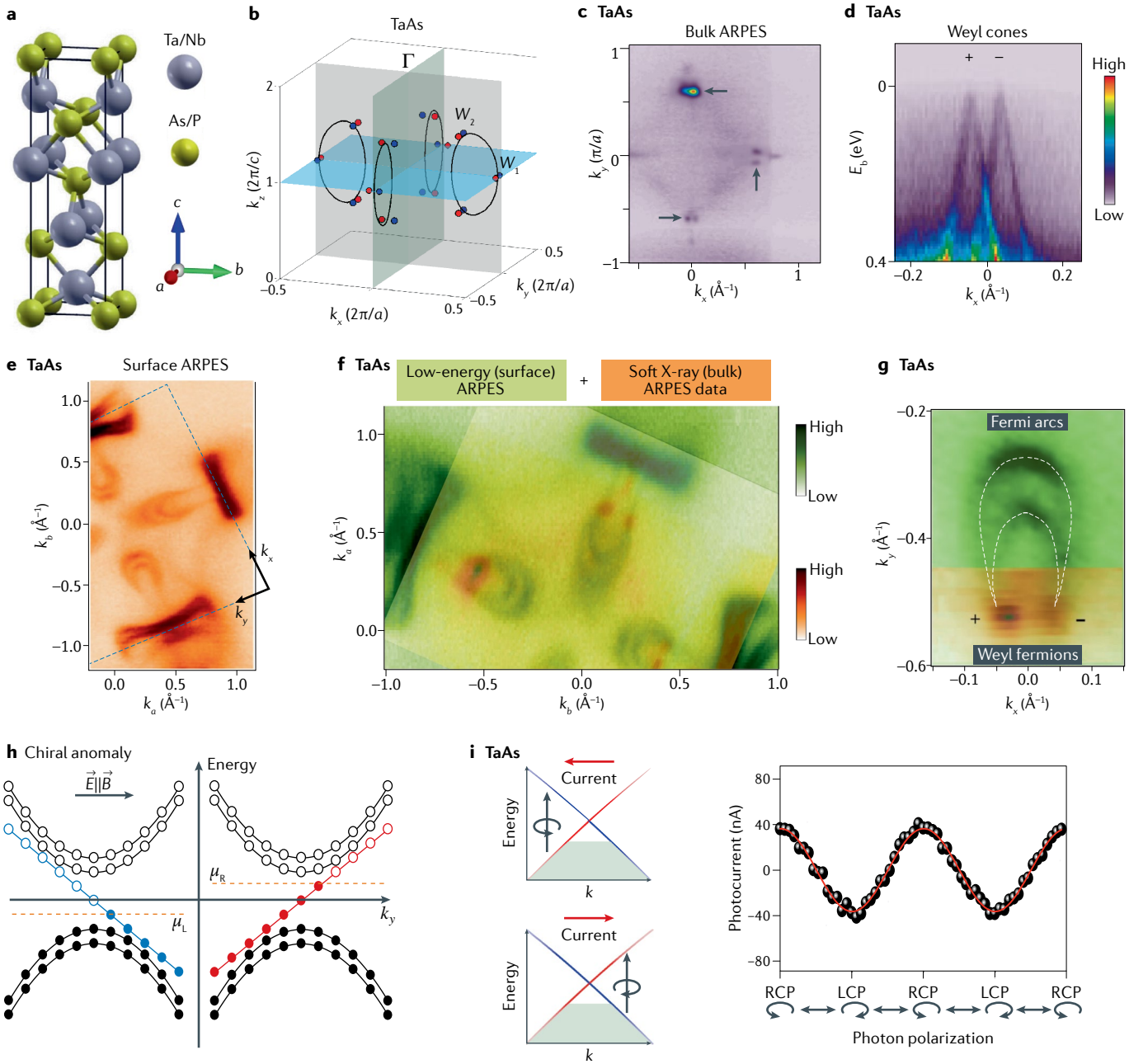

Fig. 2 | **Weyl semimetal states in the noncentrosymmetric TaAs family of crystals. a** | The crystal structure of the TaAs family breaks inversion symmetry. The lattice constants are $a = 3.437$ Å and $c = 11.656$ Å. **b** | Nodal degeneracies in TaAs in momentum space. In the absence of spin–orbit coupling, there are four nodal rings (shown in black) on the mirror planes $k_x = 0$ and $k_y = 0$. After turning on spin–orbit coupling, two groups of Weyl fermions appear: W_1 and W_2. The red and blue dots denote Weyl fermions of opposite chiral charge[30,31]. **c** | k_x–k_y Fermi surface map of the W_2 Weyl node measured by soft X-ray angle-resolved photoemission spectroscopy (SX-ARPES). **d** | E–k_x dispersion cutting through two W_2 Weyl fermions measured by SX-ARPES. Two linearly dispersive Weyl cones are observed. The colour bar indicates photoemission intensity. **e** | Electronic structure of the (001) surface of TaAs as measured by ARPES. A pair of crescent-shaped Fermi arcs are observed straddling the $\bar{\Gamma} - \bar{X}$ and $\bar{\Gamma} - \bar{Y}$ paths of the surface Brillouin zone[28,29,114–120]. **f** | The SX-ARPES map (bulk states) overlaid on the ultraviolet-ARPES-measured Fermi surface map (surface states) shows that the locations of the projected bulk Weyl fermions correspond to the terminations of the surface Fermi arcs. **g** | High-resolution ARPES maps of the Fermi arcs and Weyl fermion nodes. The dashed lines are the traces of the Fermi arcs. **h** | The chiral anomaly in Weyl semimetals. Under an applied magnetic field $\vec{B}$, the electronic structure collapses into Landau levels (indicated by the circles), which disperse in the momentum direction parallel to $\vec{B}$ (here, k_y). In the case of a Weyl semimetal, the collapse of the Weyl cones produces a set of chiral Landau levels dispersing to the left or to the right, depending on the chiral charge of the underlying Weyl fermion (blue and red circles). If an electric field is further applied, with $\vec{E}\|\vec{B}$, electrons are pumped from one chiral Landau level to the oppositely charged one. As a result, the numbers of quasiparticles with left and right chirality are not separately conserved, a phenomenon known as the chiral anomaly. **i** | Left: asymmetric excitation of a Weyl fermion under a circularly polarized laser. The photocurrents change directions when the laser sweeps from right-circular polarization (RCP) to left-circular polarization (LCP). Right: polarization-dependent photocurrents at $T = 10$ K measured in TaAs. E_b, binding energy. Panels **a** and **b** are adapted from REF.[30] CC BY 4.0 (https://creativecommons.org/licenses/by/4.0/). Panels **c**–**g** adapted with permission from REF.[28], AAAS. Panel **i** adapted from REF.[109], Springer Nature Limited.

Weyl fermions in the TaAs family[28–31,114–125]. Apart from electronic systems, Weyl excitations were also observed in gyroid photonic crystals[32].

Exotic responses of Weyl semimetals. Weyl semimetals exhibit several exotic magnetic and optical responses. One of the most fundamental examples is the chiral anomaly[18,164,165]. Historically, the chiral anomaly has been crucial in understanding many important aspects of the Standard Model of particle physics. The best-known case is the triangle anomaly associated with the decay of the neutral pion π^0 (REFS[164,165]). In condensed matter, the chiral anomaly naturally arises in Weyl semimetals[93]. Under parallel magnetic and electric fields ($\vec{E} \parallel \vec{B}$), electrons from one Weyl cone are pumped to the Weyl cone of opposite chirality, causing unbalanced charge distributions between the two Weyl cones (FIG. 2h). The resulting chiral anomaly is associated with an axial charge current leading to a negative longitudinal magnetoresistance, in which the resistivity decreases under an increasing applied magnetic field. For example, the negative magnetoresistance in the Dirac semimetal Na_3Bi suggests the existence of Weyl fermions under an external magnetic field[93]. The observation of Weyl fermions in TaAs provides a natural route to realizing the chiral anomaly in condensed matter. A strong negative magnetoresistance has been experimentally observed in the TaAs family, and was interpreted as a signature of the chiral anomaly[126–130]. However, some experimental and theoretical work has found that a negative longitudinal magnetoresistance can also be realized in crystals without Weyl fermions[166–168]. Because multiple effects can give rise to a negative longitudinal magnetoresistance, decisive experimental evidence of the chiral anomaly in Weyl semimetals has yet to emerge. A large, positive longitudinal magnetoresistance has also been observed in NbP and related systems[131,132], following analogous observations in Dirac systems[169,170] and suggesting the presence of nearly massless carriers. Further work suggested that compensated electron and hole carriers irrelevant to the topological electronic structure can also produce large, positive longitudinal magnetoresistance[133,171].

An important technique to detect the Berry curvature field of Weyl fermions is via their nonlinear optical responses. One example is the circular photogalvanic effect (CPGE), an optical response associated with photocurrents induced by circularly polarized light[106,109]. The asymmetric particle–hole excitation of a Weyl fermion creates a chirality-dependent CPGE photocurrent[106] (FIG. 2i, left). A circularly polarized photon excites only one side of the Weyl cone and generates a photocurrent that is proportional to its chiral charge. Weyl fermions of opposite chiral charge generate a photocurrent propagating in opposite directions. The sum of photocurrents from a relativistic Weyl fermion pair must vanish identically, but, owing to the small tilt of the Weyl cones in TaAs, the net photocurrent does not vanish[106,109]. It is important to note that the CPGE can also arise in the absence of Weyl fermions. To allow direct transitions within the Weyl cones while blocking transitions to/from other bands, a laser of low photon energy is used in experiments. The measured CPGE under mid-infrared lasers ($\hbar\omega = 120$ meV) oscillates with changing laser polarization (FIG. 2i, right). The CPGE photocurrent has maximum value for right-handed circularly polarized light, minimum value for a left-handed circularly polarized laser and is zero for linearly polarized light. These observations are consistent with the chirality of the Weyl fermions in TaAs (REF.[109]). Recent experiments have further observed shift currents dominated by bulk Weyl fermions in TaAs (REF.[110]). A giant anisotropic second-harmonic generation has also been observed in TaAs (REF.[108]).

Chiral charge determination. To conclude this section, we discuss how to determine the Weyl fermion chiral charge by counting Fermi arcs in ARPES. As two contrasting examples, we compare the Fermi arc surface states in the Weyl semimetal TaAs and those in the Dirac semimetal Na_3Bi (REFS[51–54]). A symmetry-protected 3D Dirac fermion is a four-fold degeneracy that can be viewed as being composed of two oppositely charged Weyl fermions[51]. As a result, each Dirac point is expected to be connected to two Fermi arcs on the surface[54]. However, the two Fermi arcs of a Dirac fermion ($C = 0$) are entirely different from the case of two Fermi arcs induced by a chiral charge $|C| = 2$. On the (100) surface of Na_3Bi (FIG. 3a), two Fermi arcs (white dotted lines) connecting the Dirac points (black dots) form a closed loop. Along a cut passing between the Dirac nodes (path β, FIG. 3b), there are two surface chiral modes (dashed lines) with opposite sign of Fermi velocity. Thus, the net chirality along the path is zero, consistent with the chiral charge of a Dirac fermion, $C = 0$. Now, we check the chiral modes of the Weyl semimetal TaAs. Two chiral modes with the same sign of Fermi velocity are observed along the loop $\mathcal{P}$ enclosing the projected Weyl fermions (FIG. 3c,d). This is consistent with the net chiral charge $|C| = 2$ enclosed in the loop. Counting the net chiral surface modes in ARPES is a powerful tool to determine the absolute value of the net Chern number. However, this method fails in ARPES when bulk pockets cross the Fermi level. For example, the net number of chiral modes along the triangular path $\mathcal{C}$ is two, inconsistent with the net charge $|C| = 3$ inside (FIG. 3e). Clear bulk states can be observed near $\overline{X}$ along the path. In this case, without accessing states above the Fermi level, one can not count the chiral edge modes along the entire loop by ARPES. Therefore, to determine the Chern number in ARPES, the energy dispersion must be fully gapped in the bulk everywhere along the chosen momentum-space path.

Type-II Weyl semimetals: LaAlGe and $Mo_xW_{1-x}Te_2$

Shortly after the observation of Weyl fermions in the TaAs family of materials, a distinct kind of Weyl fermion was theoretically proposed, termed the type-II Weyl fermion, in contrast to the Weyl fermions of TaAs, which were then referred to as type I (REFS[36,37]). The two bands forming type-II Weyl fermions have the same sign of Fermi velocity along certain directions in momentum space (FIG. 4a). Whereas type-I Weyl fermions have

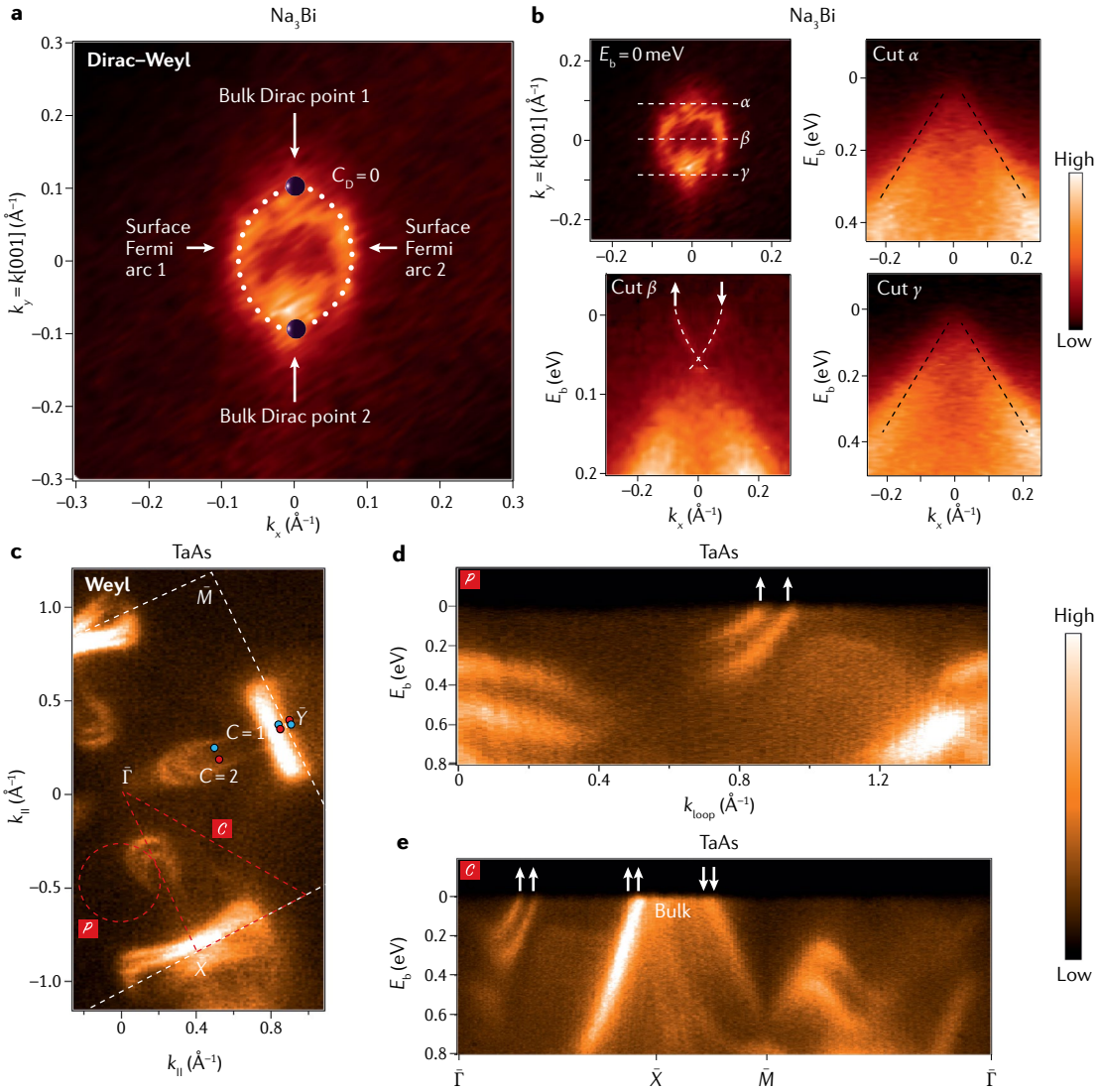

Fig. 3 | **Chern numbers and Fermi arc surface states. a** | (100) Surface states of the Dirac semimetal Na_3Bi measured by angle-resolved photoemission spectroscopy (ARPES). Two Fermi arcs (white dotted lines) connecting two bulk Dirac points (black points, Chern number $C = 0$) form a closed loop. **b** | Surface state of Na_3Bi and ARPES-measured energy dispersions along the paths α, β and γ. The white dashed lines indicate the surface Fermi arcs, with their Fermi velocities marked by arrows. The black dashed lines indicate the bulk cones. **c** | (001) Surface states of TaAs at an energy 50 meV below the Fermi level. The projected Weyl fermions on the surface are indicated by the red and blue points and the boundary of the Brillouin zone is indicated by the white dashed box. **d** | Energy dispersion along the loop $\mathcal{P}$ shown in panel **c**. The up/down arrows indicate the sign of the Fermi velocity of each band at the Fermi level. Two chiral co-propagating states are observed (as indicated by the pair of up arrows), consistent with a net charge $C = 2$ in the loop. **e** | Energy dispersion along the triangular path $\mathcal{C}$ shown in panel **c**. Bulk states pass through the Fermi level along the $\bar{X}$–$\bar{M}$ direction, making it difficult to determine the chiral surface states and related Chern numbers. E_b, binding energy. Panels **a** and **b** reprinted with permission from REF.[54], AAAS. Panels **c**–**e** reprinted with permission from REF.[119], APS.

point-like Fermi surfaces (FIG. 1e), type-II Weyl fermions have electron and hole pockets touching at a point (FIG. 4b, top). At an energy slightly off the type-II Weyl node, the electron and hole pockets disconnect, and the type-II Weyl fermion is enclosed by one of the two pockets (FIG. 4b, bottom).

The $Mo_xW_{1-x}Te_2$ family. Type-II Weyl fermions were first predicted in the $Mo_xW_{1-x}Te_2$ family of materials, space group no. 31 (REFS[36,134–136]). At the Fermi level in $Mo_xW_{1-x}Te_2$, a long arc-like feature and two large bulk projections have been observed by ARPES[137–145] (FIG. 4c). This surface state was interpreted as a topological Fermi arc due to predicted Weyl fermions. However, later research found that the arc-like surface state is topologically trivial and can exist even without Weyl fermions[141–146]. Some experiments attempted to seek other tiny arc-like features[142,143] or to resolve the states above the Fermi level by pump–probe ARPES (FIG. 4d) and STM[139,144,145]. These searches for Weyl semimetal phases in $Mo_xW_{1-x}Te_2$ typically relied heavily on the comparison between experimental measurements and

DFT calculations. According to DFT, the type-II Weyl fermions are located around 50 meV above the Fermi level, and the band inversion is on the order of 10 meV. At the Fermi level, the oppositely charged Weyl fermions merge into a trivial pocket. As a result, the Weyl semimetal phase in $Mo_xW_{1-x}Te_2$ is near a topological phase transition in first-principles calculations. For example, using slightly different lattice constants, WTe_2 was proposed to be either a trivial insulator[135] or a Weyl semimetal[36]. Similarly, depending on the size of the unit cell, $MoTe_2$ was predicted to contain either eight Weyl fermions[134] or four Weyl fermions plus extra nodal lines[136]. These different topological phases are associated with small differences in electronic structure, which are beyond the experimental resolution of ARPES measurements. Therefore, the overall agreement between theoretical calculations and experimental measurements is insufficient to determine the Weyl phase. As a result, despite intensive experimental studies, decisive evidence for type-II Weyl fermions in $Mo_xW_{1-x}Te_2$ is still lacking[137–145]. Beyond Weyl physics, WTe_2 and $MoTe_2$ have many interesting properties[147–152]. For example, large non-saturating magnetoresistance has been observed in WTe_2 (REFS[147,148]) and monolayer WTe_2 realizes the 2D quantum spin Hall effect at temperatures up to 100 K (REFS[149–152]).

The LaAlGe family. More conclusive experimental evidence of type-II Weyl fermions was observed in the LaAlGe family of materials, in the inversion-breaking space group no. 109 (REF.[146]). SX-ARPES revealed two bulk Fermi surfaces connected at two isolated points at the Fermi level (FIG. 4e, left). At a binding energy of 0.025 eV below the Fermi level, the two Fermi pockets disconnect (FIG. 4e, right). The upper and lower pockets were identified, respectively, as the hole and the electron pocket, as they respectively expand and contract with deeper binding energy. This behaviour is consistent with that of the bulk Fermi surfaces of type-II Weyl fermions (FIG. 4b). The observed node arises from the crossing between two bands with linear dispersion along all three momentum-space directions. Along the k_y direction, the Fermi velocities of the two bands have the same sign (FIG. 4f, right), again consistent with the

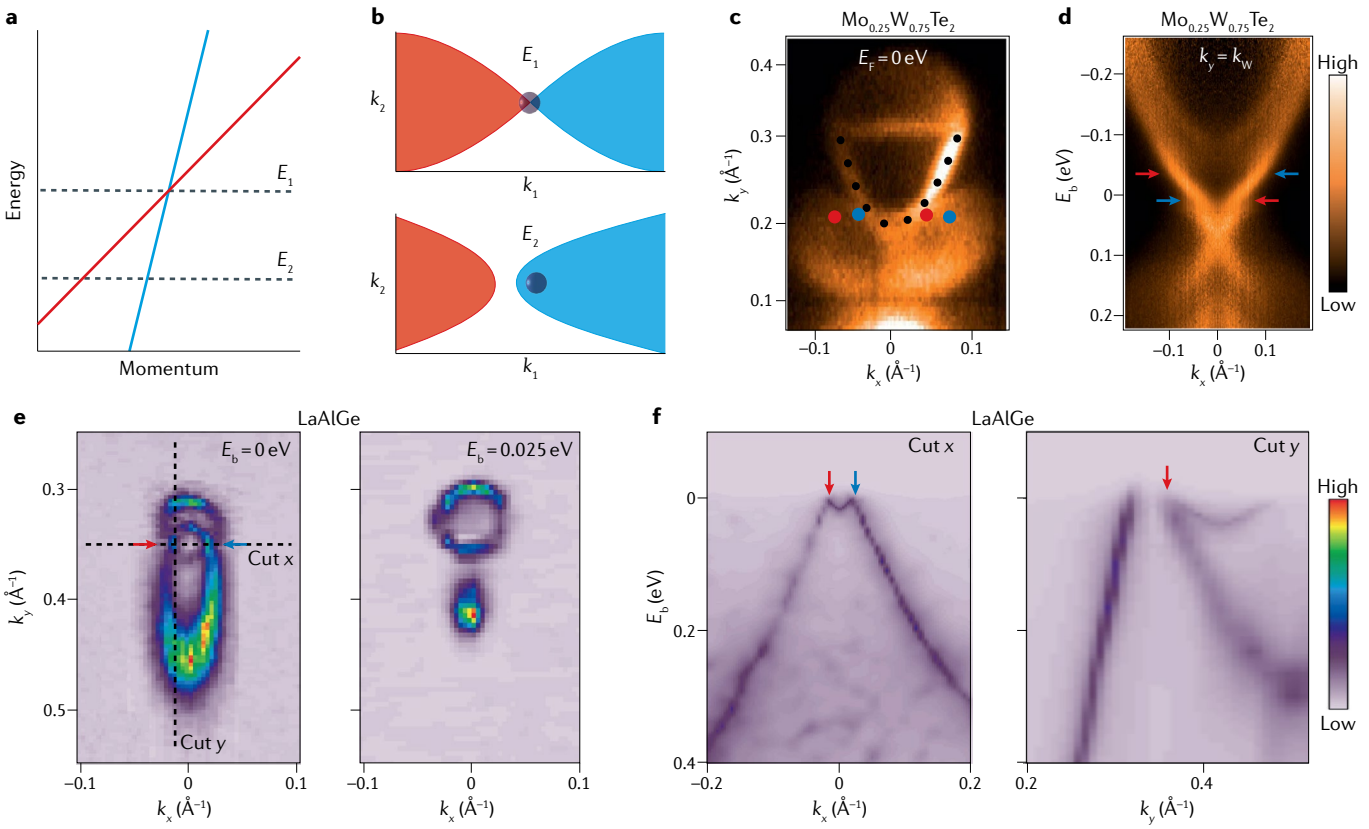

Fig. 4 | **Type-II Weyl semimetals: LaAlGe and $Mo_xW_{1-x}Te_2$. a** | Schematic of a type-II Weyl fermion. **b** | Constant-energy contours of a type-II Weyl fermion at the two energies E_1 and E_2 marked in panel **a**. The red and blue regions are the electron and the hole pocket, respectively. The black point indicates the location of the Weyl node. **c** | Fermi surface of $Mo_{0.25}W_{0.75}Te_2$ measured by angle-resolved photoemission spectroscopy. The black dots trace the topologically trivial surface arc. The red and blue points indicate the predicted position of the Weyl fermions on the surface. **d** | Energy dispersion cutting through the expected location of the Weyl points, showing kink-like features that may indicate a pair of topological Fermi arcs extending above the Fermi level and terminating on a set of four possible Weyl points (red and blue arrows, indicating the expected chiral charge of each Weyl point)[137–143]. **e** | Constant-energy contours of type-II Weyl fermions in LaAlGe. **f** | Bulk energy–momentum cuts of the type-II Weyl cones in LaAlGe. Along the k_x cut, a pair of Weyl fermions are observed (red and blue arrows, indicating the opposite chiralities assigned to these two Weyl fermions). A k_y cut through one of the Weyl fermions exhibits branches with the same sign of Fermi velocity, indicating a type-II Weyl fermion. E_b, binding energy. Panels **c** and **d** reprinted from REF.[140], CC BY 4.0 (https://creativecommons.org/licenses/by/4.0/). Panels **e** and **f** reprinted with permission from REF.[146], AAAS.

electronic structure of type-II Weyl fermions (FIG. 4a). Based on the SX-ARPES data, these observed band crossings are located at a generic point in momentum space. These data demonstrate that LaAlGe hosts type-II Weyl fermions. However, due to hybridization between the surface Fermi arcs and trivial bulk pockets, the Fermi arcs in LaAlGe were found to have weak intensity even in DFT calculations and have yet to be observed in experiments. The other two compounds in the LaAlGe family are the noncentrosymmetric magnets CeAlGe and PrAlGe (REF.[153]). This class of materials includes many varieties of Weyl fermions, including type-I, type-II, inversion-breaking and time-reversal symmetry-breaking Weyl fermions, different combinations of which coexist in the electronic structure, depending on the rare-earth element. Recent experiments have also highlighted singular angular magnetoresistance in CeAlGe, which is proposed to exhibit a switching mechanism that flips the electrical resistance for specific orientations of the magnetic field, which could be used to engineer a magnetic switch with magnetic-field-orientation-driven on/off states[154]. In PrAlGe, ARPES studies further revealed signatures of topological Fermi arc surface states, as well as the linear dispersion of the bulk Weyl fermions[172].

Topological chiral crystals in the RhSi family

Despite a growing list of experimentally observed Weyl semimetals and candidates, there remained an intense interest in developing materials with simpler electronic structures[21–27]. With a focus on Weyl semimetals arising from band inversion, first-principles calculations of a wide range of crystals found that, in most materials, Weyl fermions are too close together in momentum space, typically leading to short Fermi arcs and narrow, topologically non-trivial energy windows. Moreover, predicted band structures often exhibit a very large number of Weyl fermions scattered throughout the bulk Brillouin zone with Weyl fermions that lie far from the Fermi level, and irrelevant, trivial electron bulk and surface states at the Fermi level.

Key insights arose with a renewed focus on point touchings of bands at high-symmetry points in the Brillouin zone, which began to move the focus beyond the band-inversion picture. In principle, such symmetry-protected band crossings had been explored previously[26]. One point of view considered how high-fold degenerate band touchings in non-symmorphic space groups at high-symmetry points could be viewed as 'unconventional fermions' beyond the Weyl, Dirac and Majorana fermions well known from quantum field theory[39]. Some of these symmetry-protected, high-fold degenerate fermions at high-symmetry points were found to be Weyl-like in that they exhibit a chiral charge. Soon thereafter, it was discovered that, for symmorphic chiral space groups, time-reversal symmetry alone is sufficient to produce a Weyl point, and that, in fact, all Kramers points in these space groups pin Weyl points[40]. For non-symmorphic chiral space groups with time-reversal symmetry, the Γ point supports Kramers–Weyl fermions, whereas the Brillouin zone boundary exhibits either Kramers–Weyl fermions or chirally charged nodal surfaces, depending on the specific space group (FIG. 1f). Meanwhile, the cubic chiral space groups nos. 195–199 and nos. 207–214, which have additional symmetries, allow three-fold, four-fold and six-fold chiral fermions[39,40] (FIG. 1j). This understanding gradually eroded the prevailing intuition that Chern numbers in 3D crystals are necessarily associated with accidental band degeneracies at generic points in momentum space. Instead, Weyl fermions and their higher-fold chirally charged cousins were shown to exist universally in chiral crystal structures, and to be pinned to high-symmetry momenta. This understanding further brought to light the natural connection between the common notion of spatial chirality, or handedness, and the momentum-space chirality of a Weyl fermion[40]. Theoretical studies have also found that topological chiral crystals can exhibit many exotic electronic, optical and magnetic properties (FIG. 5a).

The RhSi family of materials. The development of topological chiral crystals immediately led to the groundbreaking prediction of a near-ideal Weyl semimetal in the RhSi family of materials[41,42]. RhSi crystallizes in the cubic, non-symmorphic chiral space group no. 198. Its electronic structure was predicted to be dominated by two higher-fold chiral fermions near the Fermi level, one at the Γ point and its oppositely charged partner at the *R* point (the corner of the bulk Brillouin zone, FIG. 5b,c), representing the largest possible momentum-space separation between two chiral charges in the Brillouin zone. Calculations of the (001) surface electronic structure further predicted giant topological Fermi arcs stretching across the entire surface Brillouin zone, from $\overline{\Gamma}$ to the corner, $\overline{M}$ (FIG. 5d, inset). Subsequent photoemission spectroscopy experiments explored the topological electronic structure of RhSi, as well as that of its isostructural cousins CoSi and AlPt (REFS[43–46]). First, measurements by surface-sensitive UV-ARPES observed surface states stretching from $\overline{\Gamma}$ to $\overline{M}$, consistent with the predicted giant topological Fermi arcs (FIG. 5d). These Fermi arcs were also demonstrated directly from the photoemission spectra by counting chiral edge modes on momentum-space loop cuts through the surface Brillouin zone, resulting in a Chern number of ±2 (REFS[43,45,46]) (FIG. 5e). These experiments also directly observed the helicoid structure of the topological surface states, with the Fermi arcs spiralling around $\overline{M}$ as a function of binding energy (FIG. 5f). Lastly, the dispersion of the Fermi arcs was found to be consistent with first-principles calculations. Complementing these surface-sensitive results, bulk-sensitive SX-ARPES experiments observed a linear electronic dispersion around the *R* point (FIG. 5c), consistent with the high-fold chiral fermions predicted in calculations. The discovery of a Weyl semimetal in the RhSi family marked a considerable advance over the first generation of Weyl semimetals. The momentum separation of the oppositely charged high-fold chiral fermions in RhSi is $\Delta = 1.16\ \text{Å}^{-1}$, an order of magnitude larger than the separation of Weyl point partners in TaAs, $\Delta = 0.07\ \text{Å}^{-1}$ (REFS[30,31,41,42]). Naturally, the associated topological Fermi arcs observed in the

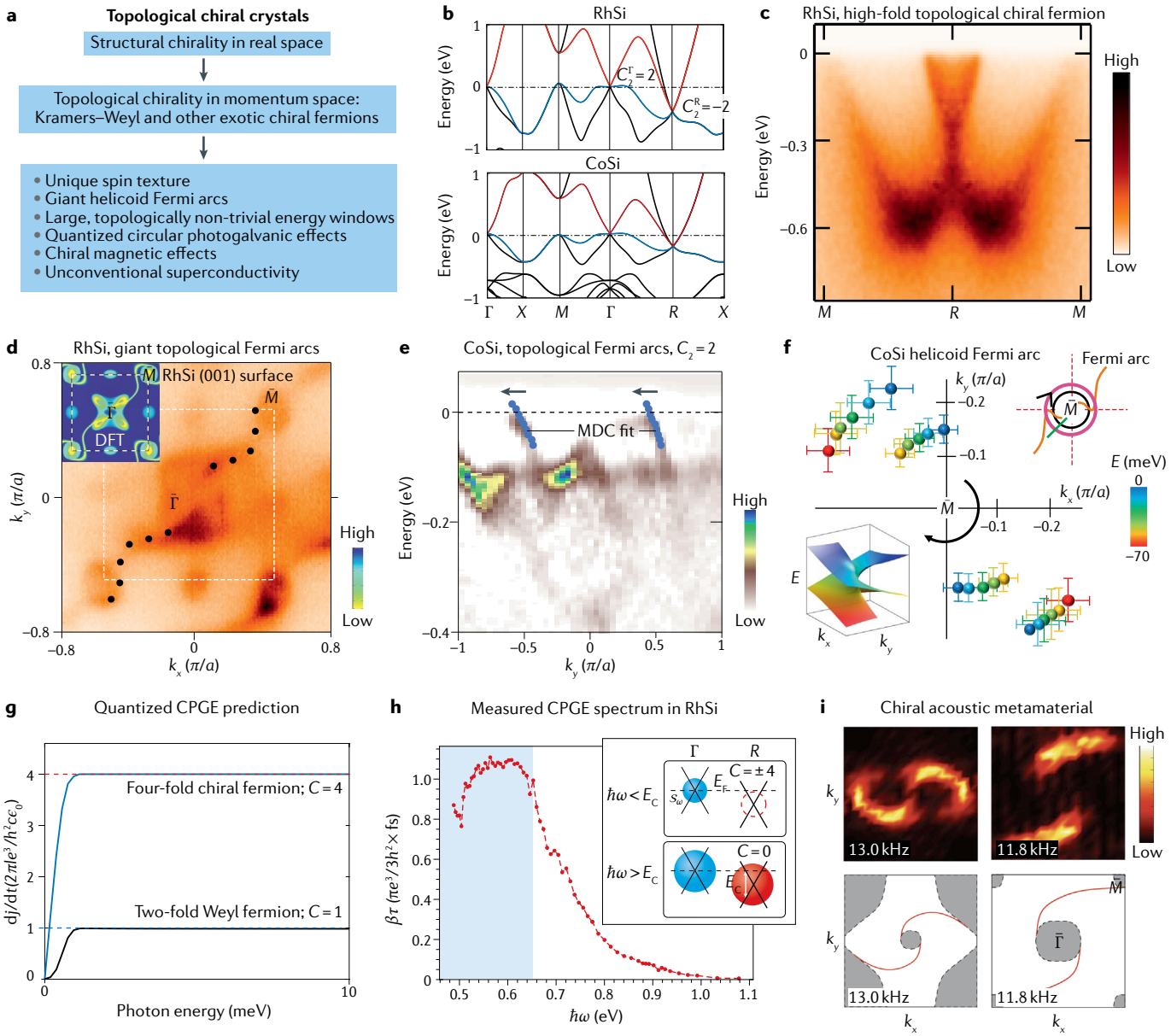

Fig. 5 | **Topological chiral crystals in the RhSi family. a** | Theoretically predicted exotic properties of topological chiral crystals. **b** | Electronic structures of CoSi and RhSi in chiral space group no. 198 in the absence of spin–orbit coupling. The Chern numbers of the three-fold chiral fermion at the Γ point are C^{Γ} = [2,2] (REFS[40–42]). **c** | Bulk cone of RhSi measured by soft X-ray angle-resolved photoemission spectroscopy (ARPES) at the *R* point. **d** | Fermi surface of RhSi measured by ARPES (white dashed line: Brillouin zone (BZ) boundary). Giant Fermi arc surface states extend diagonally across the BZ (black dots), consistent with density functional theory (DFT) calculations, shown in the inset. **e** | ARPES energy–momentum cut of CoSi through the full surface BZ, exhibiting co-propagating modes (that is, having the same sign of Fermi velocity, as indicated by the black arrows), directly demonstrating a non-zero bulk chiral charge from ARPES[43–47]. Shown is a second derivative of the ARPES photoemission intensity, with dispersion extracted by fits to photoemission momentum distribution curves (MDCs). **f** | The evolution of the Fermi arcs from deeper binding energy (red) up to the Fermi level (blue) along two loops encircling the $\overline{M}$ point (see upper inset, black and magenta loops). The arcs exhibit a helicoid structure, spiralling around $\overline{M}$ (illustrated in the lower inset). **g** | Calculation of the circular photogalvanic effect (CPGE) for a conventional two-fold Weyl fermion and a four-fold topological chiral fermion. The rate of change of the difference in photocurrent generated by left-circularly and right-circularly polarized light, dj/dt, is quantized to the Chern number of the topological fermion, in units of a combination of fundamental constants and the intensity of the applied light, *I* (*h* is Planck's constant, *e* the electron charge, ε_0 the permittivity of free space and *c* the speed of light). In these normalized units, the two-fold Weyl fermion exhibits a CPGE of 1, while the four-fold chiral fermion exhibits a CPGE of 4 (REFS[41,107]). **h** | Amplitude of the CPGE in RhSi as a function of photon energy, $\hbar\omega$. The CPGE is expressed as the product $\beta\tau$, where β is related to the CPGE tensor and τ is the lifetime of photoexcited carriers. The CPGE exhibits a plateau at low energy and decays to zero above a critical energy E_C = 0.65 eV, consistent with theoretical predictions of the quantized CPGE in RhSi. Inset: generally, optical transitions must excite occupied states to unoccupied states. Given this constraint, at energies $\hbar\omega < E_C$, only optical transitions across the topological fermion at Γ are allowed (blue sphere), indicating a non-zero quantized CPGE. However, for larger $\hbar\omega$, optical transitions across the *R* topological fermion are also allowed, giving a net *C* = 0 with zero quantized CPGE (E_F, Fermi energy)[112]. **i** | Measured isofrequency contours of the surface acoustic field distribution of a chiral acoustic metamaterial, space group no. 198. Similar to the electronic structure of RhSi, the phonon dispersion exhibits two giant Fermi arcs stretching across the surface BZ (REFS[47–50]). Panels **b**,**d**–**f** are adapted from REF.[43], Springer Nature Limited. Panel **g** reprinted with permission from REF.[41], APS. Panel **h** reprinted with permission from REF.[112], AAAS. Panel **i** reprinted from REF.[47], Springer Nature Limited.

RhSi family are also substantially longer than those observed in TaAs.

The quantized circular photogalvanic effect. Topological chiral crystals are predicted to exhibit several exotic phenomena (FIG. 5a), notably the quantized CPGE[40]. In the quantized CPGE, photocurrents produced by circularly polarized light are closely related to a universal quantity that can be written in terms of only fundamental constants and the topological chiral charge[40,41,107,112]. The quantized CPGE was first proposed in conventional two-fold Weyl semimetals[107]. Later theoretical work found that the quantized CPGE may also arise from higher-fold chiral fermions[41,173]. The theoretically simulated quantized CPGE from a two-fold Weyl fermion and four-fold chiral fermions tuned to half-filling are shown in FIG. 5g. The time derivative of the injection current is related to the Chern number in the gap. Crucially, for this effect to arise, chiral fermions of opposite chiral charge must sit at different energies in the electronic structure. This requirement excludes achiral Weyl semimetals, such as those in the TaAs family, in which the presence of mirror or other rotoinversion symmetries pairs all Weyl fermions with their oppositely charged partners at the same energy. By contrast, RhSi hosts oppositely charged high-fold chiral fermions with a large energy difference of around 0.4 eV. Furthermore, RhSi has only two chiral fermions and few irrelevant electronic states near the Fermi level, which is expected to simplify experimental studies[41]. Indeed, signatures of a topological photocurrent in RhSi and CoSi have already been reported at room temperature[112,174] (FIG. 5h). The chiral magnetic effect, a cousin of the anomalous Hall effect in which an applied magnetic field generates an electric current, similarly requires a relative energy offset of the Weyl fermions and may be explored in RhSi (REFS[94–96]).

First-principles calculations predict analogous higher-fold chiral fermions in other nonmagnetic members of the RhSi family, including RhGe, CoGe, AlPd and AuBe, as well as in the closely related BaPt*X* series, *X* = P, As, Sb (REFS[41,175]). Moreover, although recent ARPES experiments have demonstrated a chiral charge in the RhSi materials, direct spectroscopic observation of the complete topological index remains missing. To achieve this, direct observation of the *n* branches of the higher-fold chiral fermion is needed, along with the corresponding $n-1$ sets of Fermi arcs within each band gap[176]. Analogously, tuning the pump laser wavelength or sample Fermi level in a quantized CPGE experiment may also allow the observation of different quantized CPGE values associated with the distinct chiral charges of the $n-1$ band gaps[41]. The exploration of topological chiral dispersions has not been limited to electronic structures. In neighbouring communities, researchers examined the phononic structure of space group no. 198 compounds[49,50] and also fabricated acoustic metamaterials designed in the same space group[47,48]. In the acoustic metamaterials, measurements of the acoustic field distributions in the bulk demonstrated a triple point at Γ and a quadruple point at *R*, in direct analogy with the electronic structure of RhSi. On the surface of the sample, acoustic bands were observed to take the form of giant double-helicoid topological Fermi arcs, again in direct analogy with the electronic systems[47] (FIG. 5i). Topologically protected negative refraction of the Fermi arc surface states was also observed at the edge between two orthogonal neighbouring faces of the acoustic metamaterial sample. Notably, because topological Fermi arcs intrinsically have open isofrequency (constant-energy) contours, the negative refraction can take place without interfacial reflection[48]. It should similarly be possible to realize negative refraction of electrons in chiral crystals using the topological Fermi arcs in the RhSi family of materials. The large number of candidate systems and their rich topological structures offers a promising playground for future work.

Topological nodal-line semimetals

Weyl fermions and the high-fold chiral fermions discussed above are 0D topological singularities in momentum space. In condensed matter physics, topological singularities can also be higher dimensional. For instance, 1D topological nodal lines can arise where the conduction and valence bands cross along curves in momentum space, rather than at discrete points[56–69] (FIG. 6a). The appropriate topological index for a nodal line is the winding number, given by the integral of the Berry connection along a closed loop encircling the nodal line (BOX 1). The non-trivial topology of the nodal line protects drumhead surface states connecting the bulk line nodes[56–69]. Nodal-line fermions in momentum space are typically protected by certain crystal symmetries. For example, time-reversal and inversion symmetry together can protect nodal lines in the absence of SOC[58–61]. Mirror symmetry can also protect nodal lines, both in the presence and in the absence of SOC, when the bands have opposite mirror eigenvalues[58,59,62,64–69]. When time-reversal symmetry or inversion symmetry are broken, the nodal lines are two-fold degenerate and are called Weyl lines[64].

Nodal lines and drumhead surface states were first proposed in 2011 (REF.[56]). Since then, many materials have been predicted to be nodal-line semimetals, including Cu_3NZn (REF.[60]), Cu_3NPd (REF.[61]), Ca_3P_2 (REF.[62]) and $TlTaSe_2$ (REF.[63]). Most of the nodal lines predicted in the earlier studies were stabilized in the absence of SOC. After turning on SOC, these nodal lines are usually gapped out. $PbTaSe_2$ is a rare case in which Weyl lines can remain gapless even after SOC is taken into account, because mirror symmetry is preserved[64]. The band crossings of the Weyl lines along the high-symmetry lines are highlighted by the red box in FIG. 6b. The potential drumhead surface states of $PbTaSe_2$ were observed by ARPES (FIG. 6c), and the results are in good agreement with first-principles calculations. Nodal lines have also been observed in ZrSi*X* (*X* = S, Se, Te)[65,66]. According to DFT calculations, in the absence of SOC, the nodal lines in ZrSiS are protected by non-symmorphic mirror planes (top panel of FIG. 6d). In the presence of SOC, these nodal lines hybridize and open band gaps (bottom panel of FIG. 6d). Several groups have observed clear diamond-shaped nodal lines with sharp linear dispersions in ZrSi*X* (REFS[65–69]) (FIG. 6e,f).

Nodal-line networks. Recent theory has uncovered systems that host networks consisting of multiple nodal lines[70–76]. Topological nodal chains consisting of two nodal lines touching at a two-fold degenerate point (red and blue rings, FIG. 7a) were first proposed in crystals with non-symmorphic glide symmetries[70]. Later work found that Weyl and nodal chains can also be protected by symmorphic mirror planes[71]. Another unconventional 3D nodal network is the Hopf link, in which two nodal lines are linked[71–74] (red and yellow rings, FIG. 7a). The nodal knot, in which a single nodal line entangles itself, has also been theoretically proposed in toy models[75,76].

Despite the quick development of the theory of nodal-line networks, their experimental realization has been limited by the availability of material candidates. Up to now, the topological nodal chain has only been experimentally realized in photonic crystals[177]. The only material that might host Weyl-line networks with nodal-chain and Hopf-like link structures is the ferromagnetic metal Co_2MnGa (REF.[77]). Three types of Weyl lines are predicted in Co_2MnGa (blue, red and yellow lines in FIG. 7b). Generally, after taking into account SOC, the only preserved mirror plane is the one whose normal is parallel to the magnetization direction. The Weyl lines on the other mirror planes open tiny band gaps (~1 meV). Recently, both bulk Weyl lines and drumhead surface states have been observed in Co_2MnGa (REFS[77,178]). Isoenergetic contours measured by ARPES reveal the signatures of three kinds of Weyl lines in this material (FIG. 7c). FIGURE 7d,e shows the energy dispersions of the blue line nodes along the k_x direction for different k_y values. The fact that these crossings persist in a range of k_y and move in energy is consistent with the interpretation of a Weyl line. The drumhead surface states connecting the yellow Weyl lines were observed in photoemission spectra acquired along the k_{xy} direction, as shown in FIG. 7f, where the bulk cones are indicated by the yellow dots and the drumhead surface states by the green dots.

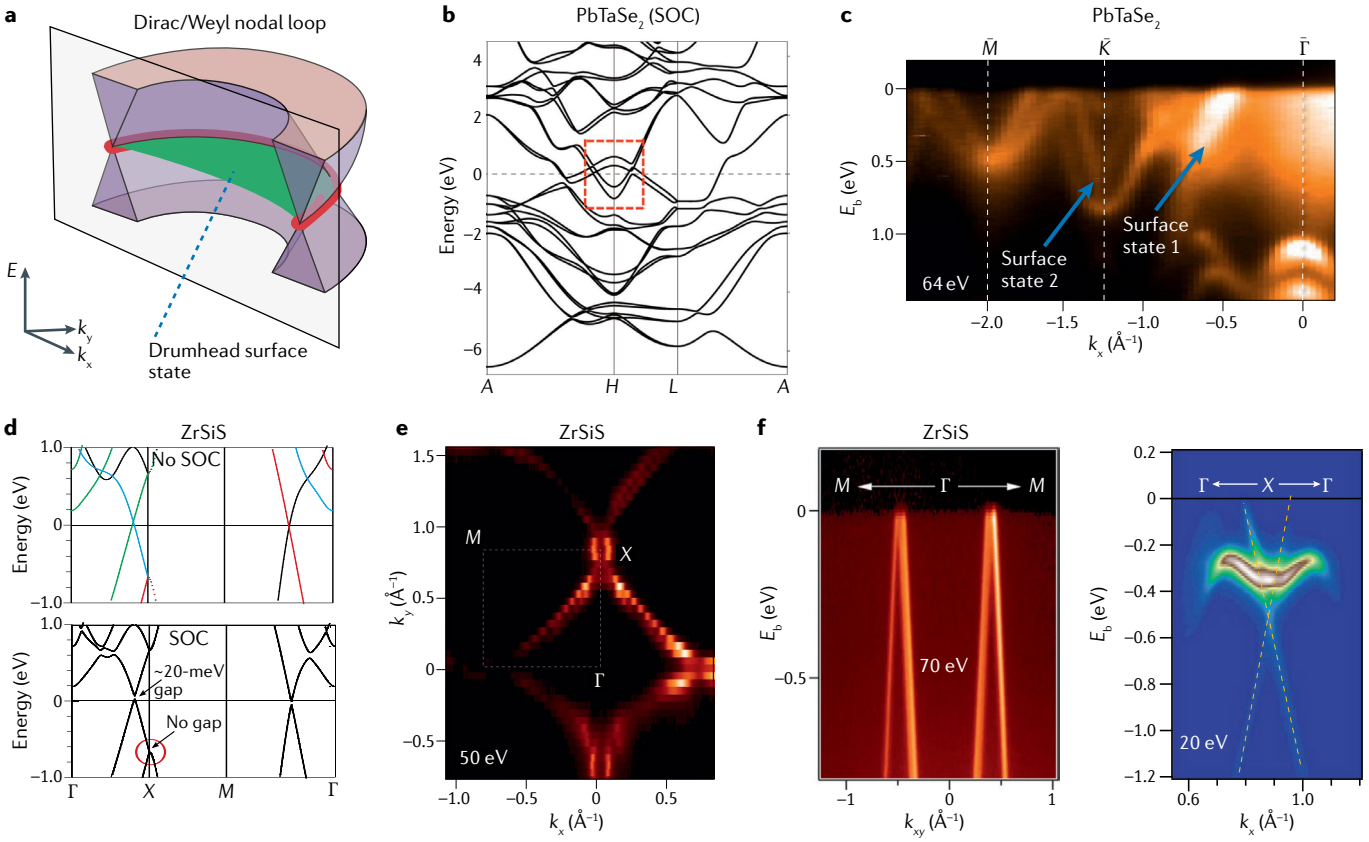

Fig. 6 | **Topological nodal lines in $PbTaSe_2$ and ZrSiS. a** | Schematic illustration of a nodal line (red) and its drumhead surface state (green). **b** | Calculated electronic structure of $PbTaSe_2$ in the presence of spin–orbit coupling (SOC). **c** | Potential drumhead surface states (indicated by the arrows) observed in $PbTaSe_2$ by angle-resolved photoemission spectroscopy. **d** | Top panel: electronic band structure of ZrSiS in the absence of SOC, indicating the different irreducible representations of the bands forming the Dirac lines. Bottom panel: in the presence of SOC, small gaps open in the Dirac lines, but the overall electronic structure remains the same. **e** | Fermi surface of ZrSiS measured by angle-resolved photoemission spectroscopy. The diamond-shaped contour is a Dirac nodal line. **f** | Left: the energy–momentum cut through the Dirac nodal line exhibits a cone dispersion with an apparent crossing point slightly above the Fermi level, consistent with density functional theory calculations. Right: additional cone dispersions were observed away from the Dirac nodal line, at the boundary of the Brillouin zone, and were identified with a band crossing at the *X* point. E_b, binding energy. Panel **a** reprinted with permission from REF.[77], AAAS. Panels **b** and **c** reprinted from REF.[64], CC BY 4.0 (https://creativecommons.org/licenses/by/4.0/). Panels **d** and **f** (right) adapted from REF.[65], CC BY 4.0 (https://creativecommons.org/licenses/by/4.0/). Panels **e** and **f** (left) reprinted with permision from REF.[66], APS.

Anomalous Hall and Nernst effects. Recent work suggests that Weyl lines are exceptionally effective at producing large and robust anomalous Hall and Nernst effects (AHEs and ANEs, respectively). Co_2MnGa exhibits the largest ANE known, reaching 6 V K^{-1} at room temperature and, thus, exceeding other magnetic conductors by one order of magnitude[179,180]. The AHE in Co_2MnGa, of order $10^3\ \Omega^{-1}\,cm^{-1}$, is also among the largest known

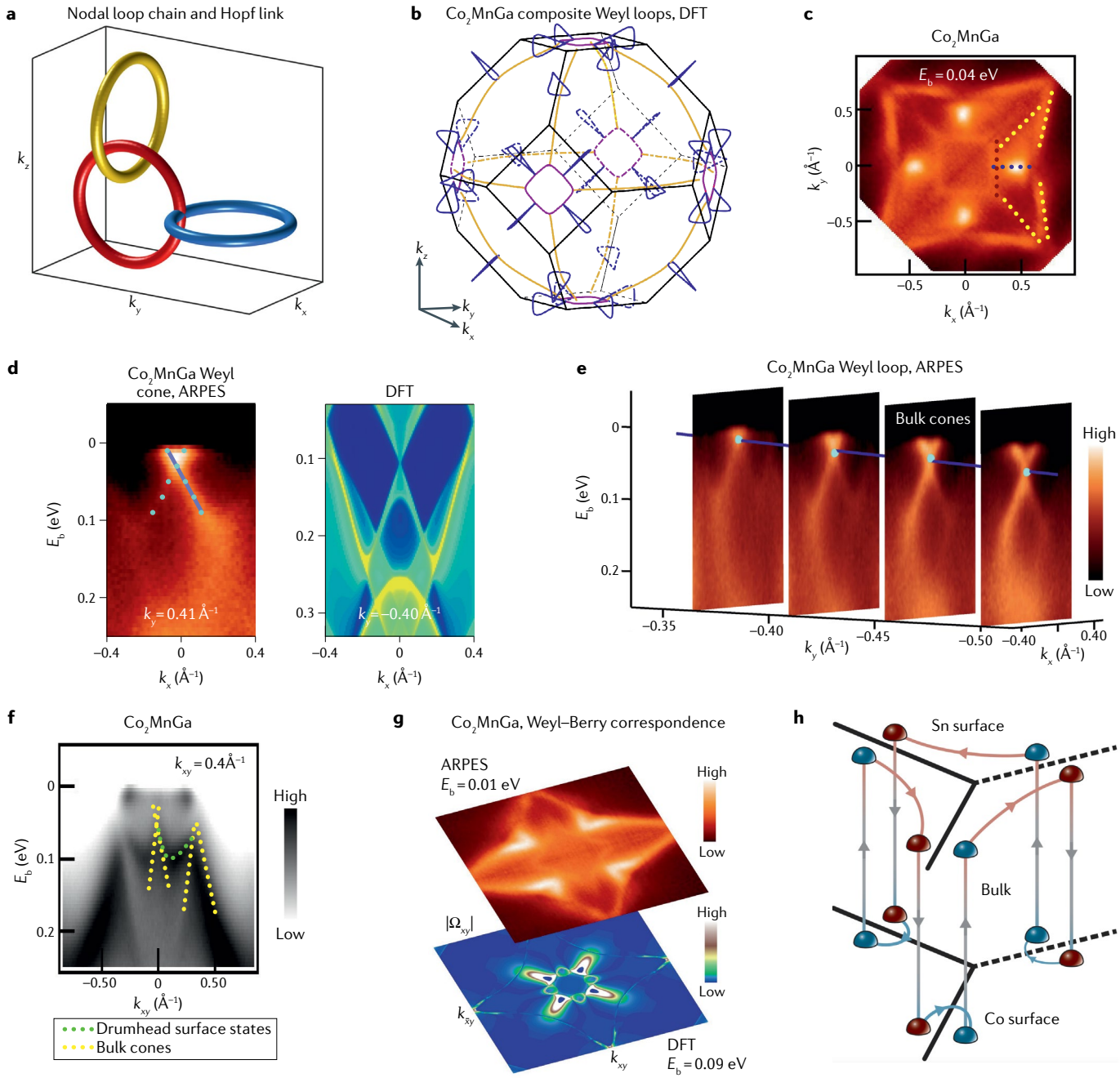

Fig. 7 | **Magnetic Weyl lines and drumhead surface states in Co_2MnGa.** **a** | Nodal lines naturally form rich composite structures, including links (illustrated for the case of a Hopf link formed by the yellow and red nodal lines) and chains (formed by the red and blue nodal lines). **b** | The Weyl-line network in the momentum space of Co_2MnGa as predicted by density functional theory (DFT). **c** | Fermi surface measured by angle-resolved photoemission spectroscopy (ARPES) at a binding energy $E_b = 0.04$ eV. The coloured dots correspond to the different Weyl lines in panel **b**. **d** | Left: ARPES energy–momentum cut obtained along k_x at fixed k_y, showing a cone dispersion centred on a crystallographic mirror plane (mirror plane located at $k_x = 0\ Å^{-1}$). Right: Analogous energy–momentum cut obtained by DFT, showing a Weyl-line cone arising from the blue Weyl line. **e** | By examining a series of ARPES energy–momentum cuts obtained at different values of k_y, one can see that the cone dispersion of panel **d** persists as k_y varies. This result is inconsistent with a point touching of bands and, rather, indicates a line touching protected by mirror symmetry. This line touching is indicated by the blue Weyl line. **f** | Energy dispersion along $k_{\bar{x}y} = 0.4\ Å^{-1}$ measured by ARPES. The yellow dots highlight the Weyl cones along one of the yellow Weyl lines in panel **b**. The additional states connecting the Weyl-line nodes are the drumhead surface states (green dots). **g** | Top: ARPES-measured constant-energy contour at $E_b = 0.01$ eV on the (001) surface. Bottom: the calculated Berry curvature field intensity. The correspondence between ARPES and DFT suggests that the Weyl lines concentrate Berry curvature in the electronic structure. **h** | Schematic of three pairs of Weyl fermions and their Fermi arcs in $Co_3Sn_2S_2$. Panel **b** reprinted with permission from REF.[71], APS. Panels **c**–**g** reprinted with permission from REF.[77], AAAS. Panel **h** reprinted with permission from REF.[188], AAAS.

and persists to room temperature[77,181]. A scaling analysis of the AHE as a function of temperature, combined with ARPES measurements of the Weyl lines and first-principles calculations, suggests that the Berry curvature concentrated by the Weyl lines drives the giant AHE in Co_2MnGa (REF.[77]) (FIG. 7g). This represents a considerable success in achieving robust, high-temperature transport driven by topological electronic structures. Fe_3Ga and Fe_3Al, which crystallize in the same space group as Co_2MnGa, were also shortly thereafter observed to host a giant ANE, reaching 4–5 $V K^{-1}$ at room temperature[182]. Through first-principles calculations, this giant ANE was attributed to the Berry curvature field generated by a rich Weyl-line network extending throughout the bulk Brillouin zone. Apart from Co_2MnGa and the Fe_3Ga family, the van der Waals ferromagnet Fe_3GeTe_2 was also found to exhibit a large AHE, which, again, was attributed to topological Weyl lines[183].

A giant AHE was also observed in the kagome magnet $Co_3Sn_2S_2$. First-principles calculations predicted that $Co_3Sn_2S_2$ hosts three topological Weyl lines in the absence of SOC[184–186] and that, under SOC, these Weyl lines gap out, leaving behind three pairs of Weyl points 60 meV above the Fermi level. Subsequent works explored the predicted Weyl points by ARPES and STM, relying on comparison with first-principles calculations to interpret certain bulk and surface states as signatures of Weyl points and topological Fermi arcs[187,188] (FIG. 7h). A large zero-field ANE was also reported in $Co_3Sn_2S_2$ (REF.[189]). At the same time, calculations predicted a large Berry curvature associated with the SOC-gapped Weyl lines at the Fermi level, and an AHE with maximum value very close to the Fermi level and a steep drop moving towards the Weyl point energy[184]. As a result, some works suggested that the large AHE and ANE arise predominantly due to Berry curvature concentrated by the Weyl lines[189–191].

The community has also given considerable attention to Fe_3Sn_2 and the Mn_3Sn family of topological magnets, which also exhibit a large AHE and ANE. However, for these materials, the Berry curvature is thought to be concentrated by massive Dirac fermions, in the case of Fe_3Sn_2 (REFS[192,193]), and Weyl points, in the case of Mn_3Sn (REFS[194–197]). To determine the origin of the large AHE and ANE in topological magnets, spectroscopic measurements are a powerful tool. The future will, no doubt, see the discovery of many other examples of anomalous transport arising from topological electronic structures.

Outlook

The materials discussed in this Review represent only a small fraction of the candidate topological conductors known to the community. As a helpful guide to the field, we list some of the predicted Weyl materials, along with the current experimental status, in TABLE 1. First-principles calculations continue to play a crucial role in the search for new topological quantum materials. Some predictions have been experimentally confirmed, such as the presence of Weyl fermions and their high-fold analogues in the TaAs and RhSi families of materials, respectively. Thanks to rapidly increasing computational power, material predictions have also greatly accelerated. For example, thousands of potential topological materials were predicted very recently[198–200]. However, identifying the most promising candidates involves avoiding the pitfalls of first-principles calculations[201]. Most existing predictions lack conclusive evidence; thus, more detailed calculations, as well as further experimental studies, will be needed. As highlighted by Alex Zunger[201], it is important to check theoretically and experimentally that the material is stable in the desired crystal structure, possesses the required magnetic order, can be synthesized with sufficiently high crystalline quality, remains robust upon any required doping, has well-characterized electron–electron interactions and so on. Such considerations are even more important for topological phases relying on specific magnetic orders or other interacting phenomena, which can complicate first-principles calculations. Going forward, the search for high-quality topological materials and exotic new topological states of matter will benefit more than ever from close collaboration between theoretical and experimental techniques.

One of the new frontiers in the exploration of topological materials is topological magnets with rich magnetic tunability. The ideal topological quantum materials host topological indices accompanied by a large Berry curvature field at the Fermi level. The interplay between the magnetic field and the giant Berry curvature field can induce many exotic quantum phenomena[202,203]. Here, we use kagome magnets as an example (FIG. 8a), which have an electronic structure consisting of a flat band and massless Dirac fermions (FIG. 8b). As a first example, we consider the anomalous magnetic response of the half-metallic kagome magnet $Co_3Sn_2S_2$ (REF.[204]). This material features a spin-polarized kagome flat band at the Fermi level, which appears as a sharp peak in the density of states (FIG. 8c). Under an external magnetic field, this flat-band peak exhibits an anomalous energy shift in the direction opposite to that of the applied field (FIG. 8d). This negative magnetic moment of the flat band is related to the underlying Berry curvature field. As a second example, the kagome magnet Fe_3Sn_2 exhibits a large and anisotropic magnetic field response[193]. The system exhibits massive Dirac bands whose gap can be tuned by an external magnetic field[192] (FIG. 8e). The response is large, with an effective g-factor of over 100, two orders of magnitude larger than that of the conventional electron spin. More unexpectedly, the electronic structure shows intricate nematicity, which can be systematically rotated by the vector magnetization (FIG. 8f). The exotic magnetic tunability of topological quantum materials[205–207] offers a path to topologically protected spintronic applications in the areas of magnetic sensors and electromagnetic converters.

Magnetic topological crystals have also opened new frontiers for the observation of quantized electromagnetic responses. One example is the quantum anomalous Hall effect (QAHE), a phenomenon arising in 2D magnetic materials in which the transverse conductivity is quantized to integer multiples of the conductance quantum, e^2/h. In existing setups, this effect persists to temperatures of only several Kelvin[208]. One approach to develop new QAHE materials considers thin films

Table 1 | **Theoretical predictions and experimental investigations of Weyl material candidates**

Material	Theoretical predictions	Spectroscopy measurements	Magnetic and optical responses in experiments	Remarks
TaAs family	I-breaking; 24 Weyl fermions[30,31]	ARPES and STM[28,29,114–125]	Negative longitudinal magnetoresistance[126–133]; nonlinear optical responses[108–110]	First experimentally demonstrated Weyl semimetal
RhSi family	I-breaking; two high-fold chiral fermions[40–42,49]	ARPES[43–46,50]	Quantized circular photogalvanic effects[112]	Confirmed as nearly ideal Weyl semimetals
LaAlGe	I-breaking; 40 Weyl fermions[146]	ARPES[146]	Not reported	Type-II Weyl cones observed; Fermi arcs data needed
$W_{1-x}Mo_xTe_2$	I-breaking; eight Weyl fermions[36,134,135]	ARPES and STM[137–142,144,145]	Negative longitudinal magnetoresistance[210]	Weyl fermions predicted above the Fermi level; clear type-II bulk cone data needed
$TaIrTe_4$	I-breaking; four Weyl fermions[211]	ARPES[212,213]	Preliminary transport[214]; nonlinear optical responses[111]	Weyl fermions predicted above the Fermi level; clear type-II bulk cone data needed
WP_2, MoP_2	I-breaking; eight Weyl fermions[215]	ARPES[171]	Preliminary transport[216]	Direct experimental evidence of Weyl fermions needed
PrAlGe, CeAlGe	T-breaking & I-breaking[153]	ARPES[172]	Singular angular magnetoresistance[154]	Signatures of a magnetic Weyl state
Mn_3Ge, Mn_3Sn	Noncollinear antiferromagnetic Weyl semimetal[197]	ARPES[196]	Strong anomalous Hall effect[194,195]	Direct observation of Weyl fermions and Fermi arcs needed
$Co_3Sn_2S_2$	Ferromagnetic Weyl semimetal[184–188,191]	ARPES and STM[184–186]	Strong anomalous Hall effect[184,185]	Kagome flat bands detected[204]; Weyl fermions predicted above the Fermi level
$TlBi(S_{0.5}Se_{0.5})_2$	I-breaking[217]	Not reported	Not reported	–
HgTe/CdTe superlattice	I-breaking; eight Weyl fermions[218]	Not reported	Not reported	–
$LaBi_{1-x}Sb_xTe_3$ family	I-breaking; 12 Weyl fermions[219]	Not reported	Not reported	–
BiTeI	I-breaking;12 Weyl fermions[219]	Not reported	Not reported	–
Te and Se in the trigonal phase	I-breaking[220]	Not reported	Not reported	High pressure required
$SrSi_2$	I-breaking; double Weyl[159]	Not reported	Not reported	–
Ta_3S_2	I-breaking; 40 Weyl fermions[221]	Not reported	Preliminary transport measurements[222]	–
$CuTlSe_2$ family	I-breaking; eight Weyl fermions[223]	Not reported	Not reported	–
β-Bi_4Br_4 family	I-breaking; four Weyl fermions[224]	Not reported	Not reported	High pressure required
Ag_2Se	I-breaking; Kramers–Weyl fermions[40]	Not reported	Negative longitudinal magnetoresistance[225]	–
$R_2Ir_2O_7$	T-breaking; 24 Weyl fermions[33]	Not reported	Not reported	Magnetic structure inconclusive[160,161]
TI/FM insulator superlattice	T-breaking; two Weyl fermions[34]	ARPES[162]	Not reported	Topological phase transition in Bi_2Se_3-based non-magnetic superlattice[162]
$HgCr_2Se_4$	T-breaking; double Weyl fermions[158]	Not reported	Not reported	–
$Bi_{0.97}Sb_{0.03}$	T-breaking[226]	Not reported	Negative longitudinal magnetoresistance[226]	External magnetic field required
$Hg_{1-x-y}Cd_xMn_yTe$	T-breaking; two Weyl fermions[227]	Not reported	Not reported	External magnetic field required
$YbMnBi_2$	T-breaking[228]	ARPES[228]	Not reported	Magnetic order needs further confirmation[228]
CeSbTe	T-breaking[229]	Not reported	Preliminary transport measurements[229]	Direct observation of Weyl fermions and Fermi arcs needed
GdPtBi	T-breaking[230]	Not reported	Negative longitudinal magnetoresistance[230]	External magnetic field required
Magnetic Heusler materials XCo_2Z (X = IVB or VB; Z = IVA or IIIA)	T-breaking[231,232]	Not reported	Not reported	–
SrPtAs	T-breaking; superconducting[233]	Not reported	Not reported	μSR suggested a T-breaking superconducting pairing; T_c = 2.4 K (REF.[234])
URu_2Si_2	T-breaking; two Weyl fermions; superconducting[235]	Not reported	Not reported	–
B-phase of UPt_3	T-breaking; superconducting[236]	Not reported	Not reported	–
Li_2Pd_3B	I-breaking; Kramers–Weyl fermions; superconducting[40]	Not reported	Not reported	–

A list of predicted inversion-breaking ($\mathcal{I}$-breaking) and time-reversal-breaking ($\mathcal{T}$-breaking) Weyl semimetal candidates. For most of them, conclusive experimental evidence is still lacking. μSR, muon spin resonance; ARPES, angle-resolved photoemission spectroscopy; FM, ferromagnet; STM, scanning tunnelling microscopy; T_c, superconducting critical temperature; TI topological insulator.

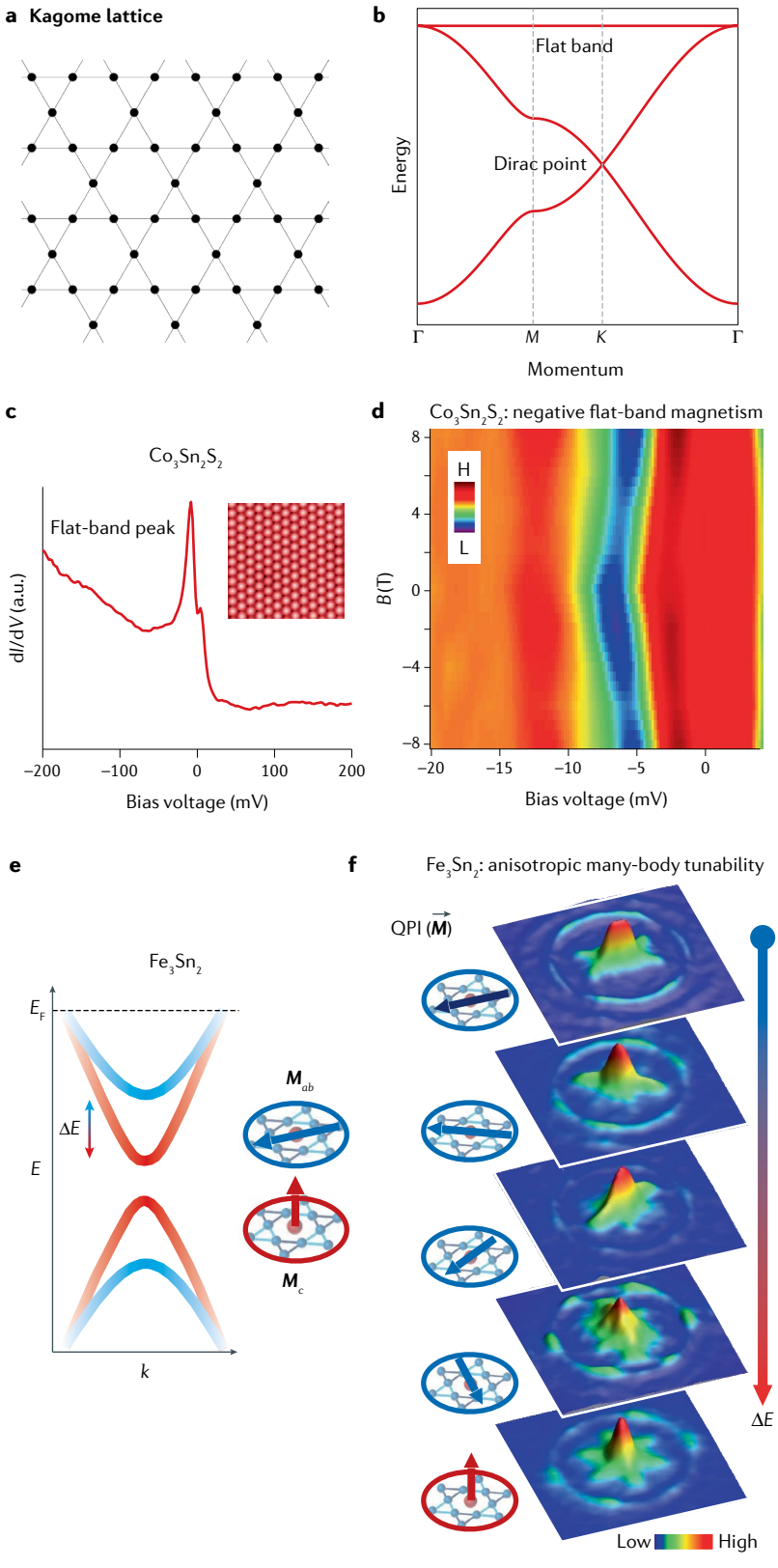

Fig. 8 | **Magnetic tunability of topological kagome magnets. a** | Illustration of a kagome lattice. **b** | Band structure of a kagome lattice with a flat band and a Dirac point. **c** | Tunnelling spectrum on the S surface (inset) of $Co_3Sn_2S_2$, showing the pronounced kagome flat-band peak. **d** | Second derivative of the tunnelling spectrum as a function of applied *c*-axis magnetic field *B*. The peak shifts in energy by the same amount and in the same direction for both orientations of the magnetic field. The derived magnetic moment value is $m \approx -3\ \mu_B$. **e** | Schematic of the magnetization-controlled Dirac gap in the kagome lattice of Fe_3Sn_2. E_F is the Fermi energy, and M_{ab} and M_c are the magnetization in the *a*–*b* plane and along the *c*-axis, respectively. **f** | Quasiparticle interference (QPI) patterns of Fe_3Sn_2 as a function of the magnetization direction, which is indicated in the insets. The uppermost QPI pattern shows spontaneous nematicity along the *a*-axis. Magnetization along other directions can alter, and, thus, control, the electronic symmetry. Detailed angle-resolved photoemission spectroscopy measurements of massive Dirac fermions in Fe_3Sn_2 can been found in REF.[192]. Panels **c** and **d** are adapted from REF.[204], Springer Nature Limited. Panels **e** and **f** adapted from REF.[193], Springer Nature Limited.

of magnetic Weyl semimetals, rather than topological insulators. The large anomalous Hall response observed in topological magnets[77,89,179–181,183–188,192,194–197,204] also naturally motivates the search for a 3D QAHE. This phase can be viewed as a stack of ordinary 2D QAHE states or, alternatively, as a phase that arises when a magnetic Weyl semimetal is tuned in such a way that all Weyl points annihilate one another. A 3D QAHE state may provide quantized conductance at high temperatures while circumventing the experimental challenges of working with a 2D device. Lastly, it has recently been proposed that, under certain conditions, the linking number of the Weyl lines in an electronic structure may determine the quantized θ angle of the axion Lagrangian[74], suggesting that new topological mechanisms for quantized electromagnetic responses still wait to be explored.

The electromagnetic field and nonlinear optical responses of thin films of topological semimetals might open a new direction. Compared with bulk crystals, thin films of topological materials, in which surface states may dominate, can have different electronic, magnetic and optical properties. For example, subject to external magnetic fields, Fermi arcs on opposite surfaces of the sample play a key role in the quantum Hall effect in Cd_3As_2 thin films[103]. Also, thin films of the topological chiral crystal RhSi illuminated by circularly polarized light are predicted to exhibit Fermi arc surface photogalvanic currents flowing perpendicular to bulk injection currents, potentially allowing novel functionality[113].

Novel superconducting and correlated topological phases also lie on the horizon. In RhSi, the large separation of the high-fold chiral fermions in momentum space may offer the possibility of engineering new kinds of unconventional superconductivity via doping or proximity effects[84–88]. Magnetic topological materials, including kagome materials with flat bands, may also enable the exploration of interacting topological phases, including fractional topological states[209]. The theoretical and experimental advances needed to realize such exotic states of matter will, no doubt, emerge as an important future direction for the field.

Published online: 26 April 2021

1. Weyl, H. Elektron und gravitation. I. *Z. Phys.* **56**, 330–352 (1929).
2. Wilczek, F. Why are there analogies between condensed matter and particle theory? *Phys. Today* **51**, 11–13 (1998).
3. Anderson, P. W. *Concepts in Solids: Lectures on the Theory of Solids* (World Scientific, 1997).
4. Thouless, D. J. *Topological Quantum Numbers in Nonrelativistic Physics* (World Scientific, 1998).
5. Neto, A. H. C. et al. The electronic properties of graphene. *Rev. Mod. Phys.* **81**, 109 (2009).
6. Hasan, M. Z. & Kane, C. L. Topological insulators. *Rev. Mod. Phys.* **82**, 3045–3067 (2010).
7. Qi, X.-L. & Zhang, S.-C. Topological insulators and superconductors. *Rev. Mod. Phys.* **83**, 1057–1110 (2011).
8. Vafek, O. & Vishwanath, A. Dirac fermions in solids: from high-T_c cuprates and graphene to topological insulators and Weyl semimetals. *Annu. Rev. Condens. Matter Phys.* **5**, 83–112 (2014).
9. Hasan, M. Z., Xu, S.-Y. & Bian, G. Topological insulators, topological superconductors and Weyl fermion semimetals. *Phys. Scr.* **2015**, 014001 (2015).
10. Turner, A. M. & Vishwanath, A. in *Topological Insulators: Fundamentals and Perspectives* (eds Ortmann, F., Roche, S. & Valenzuela, S. O.) (Wiley, 2015).
11. Bansil, A., Lin, H. & Das, T. Topological band theory. *Rev. Mod. Phys.* **88**, 021004 (2016).
12. Weng, H., Dai, X. & Fang, Z. Topological semimetals predicted from first-principles calculations. *J. Phys. Condens. Matter* **28**, 303001 (2016).
13. Haldane, F. D. M. Nobel lecture: Topological quantum matter. *Rev. Mod. Phys.* **89**, 040502 (2017).
14. Weyl, H. *Gesammelte Abhandlungen II* (American Philosophical Society, 1943).
15. von Neumann, J. & Wigner, E. P. Über das verhalten von eigenwerten bei adiabatischen prozessen. *Phys. Z.* **30**, 467–470 (1929).
16. Herring, C. Accidental degeneracy in the energy bands of crystals. *Phys. Rev.* **52**, 365–373 (1937).
17. Abrikosov, A. A. & Beneslavskii, S. D. Some properties of gapless semiconductors of the second kind. *J. Low Temp. Phys.* **5**, 141–154 (1971).
18. Nielsen, H. B. & Ninomiya, M. The Adler-Bell-Jackiw anomaly and Weyl fermions in a crystal. *Phys. Lett. B* **130**, 389–396 (1983).
19. Volovik, G. E. *The Universe in a Helium Droplet* (Clarendon Press, 2003).
20. Murakami, S. Phase transition between the quantum spin Hall and insulator phases in 3D: emergence of a topological gapless phase. *New J. Phys.* **9**, 356 (2007).
21. Jia, S., Xu, S.-Y. & Hasan, M. Z. Weyl semimetals, Fermi arcs and chiral anomalies. *Nat. Mater.* **15**, 1140–1144 (2016).
22. Burkov, A. A. Topological semimetals. *Nat. Mater.* **15**, 1145–1148 (2016).
23. Hasan, M. Z. et al. Discovery of Weyl fermion semimetals and topological Fermi arcs. *Annu. Rev. Condens. Matter Phys.* **8**, 289–309 (2017).
24. Yan, B. & Felser, C. Topological materials: Weyl semimetals. *Annu. Rev. Condens. Matter Phys.* **8**, 338–354 (2017).
25. Zheng, H. & Hasan, M. Z. Quasiparticle interference on type-I and type-II Weyl semimetal surfaces: a review. *Adv. Phys. X* **3**, 146661 (2018).
26. Armitage, N. P., Mele, E. J. & Vishwannath, A. Weyl and Dirac semimetals in three-dimensional solids. *Rev. Mod. Phys.* **90**, 015001 (2018).
27. Hu, J., Xu, S.-Y., Ni, N. & Mao, Z. Transport of topological semimetals. *Annu. Rev. Mater. Res.* **49**, 207–252 (2019).
28. Xu, S.-Y. et al. Discovery of a Weyl fermion semimetal and topological Fermi arcs. *Science* **349**, 613–617 (2015).
29. Lv, B. Q. et al. Experimental discovery of Weyl semimetal TaAs. *Phys. Rev. X* **5**, 031013 (2015).
30. Huang, S. M. et al. A Weyl fermion semimetal with surface Fermi arcs in the transition metal monopnictide TaAs class. *Nat. Commun.* **6**, 7373 (2015).
31. Weng, H., Fang, C., Fang, Z., Bernevig, A. & Dai, X. Weyl semimetal phase in non-centrosymmetric transition metal monophosphides. *Phys. Rev. X* **5**, 011029 (2015).
32. Lu, L. et al. Experimental observation of Weyl points. *Science* **349**, 622–624 (2015).
33. Wan, X., Turner, A. M., Vishwanath, A. & Savrasov, S. Y. Topological semimetal and Fermi-arc surface states in the electronic structure of pyrochlore iridates. *Phys. Rev. B* **83**, 205101 (2011).
34. Burkov, A. A. & Balents, L. Weyl semimetal in a topological insulator multilayer. *Phys. Rev. Lett.* **107**, 127205 (2011).
35. Balents, L. Weyl electrons kiss. *Physics* **4**, 36 (2011).
36. Soluyanov, A. A. et al. Type-II Weyl semimetals. *Nature* **527**, 495–498 (2015).
37. Xu, Y., Zhang, F. & Zhang, C. Structured Weyl points in spin-orbit coupled fermionic superfluids. *Phys. Rev. Lett.* **115**, 265304 (2015).
38. Mañes, J. L. Existence of bulk chiral fermions and crystal symmetry. *Phys. Rev. B* **85**, 155118 (2012).
39. Bradlyn, B. et al. Beyond Dirac and Weyl fermions: unconventional quasiparticles in conventional crystals. *Science* **353**, aaf5037 (2016).
40. Chang, G. et al. Topological quantum properties of chiral crystals. *Nat. Mater.* **17**, 978–985 (2018).
41. Chang, G. et al. Unconventional chiral fermions and large topological topological Fermi arcs in RhSi. *Phys. Rev. Lett.* **119**, 206401 (2017).
42. Tang, P., Zhou, Q. & Zhang, S.-C. Multiple types of topological fermions in transition metal silicides. *Phys. Rev. Lett.* **119**, 206402 (2017).
43. Sanchez, D. S. et al. Topological chiral crystals with helicoid-arc quantum states. *Nature* **567**, 500–505 (2019).
44. Zhao, R. et al. Observation of unconventional chiral fermions with long Fermi arcs in CoSi. *Nature* **567**, 496–499 (2019).
45. Takane, D. et al. Observation of chiral fermions with a large topological charge and associated Fermi-arc surface states in CoSi. *Phys. Rev. Lett.* **122**, 076402 (2019).
46. Schröter, N. B. M. et al. Chiral topological semimetal with multifold band crossings and long Fermi arcs. *Nat. Phys.* **15**, 759–765 (2019).
47. Yang, Y. et al. Topological triply degenerate point with double Fermi arcs. *Nat. Phys.* **15**, 645–649 (2019).
48. He, H. et al. Topological negative refraction of surface acoustic waves in a Weyl phononic crystal. *Nature* **560**, 61–64 (2018).
49. Zhang, T. et al. Double-Weyl phonons in transition-metal monosilicides. *Phys. Rev. Lett.* **120**, 016401 (2018).
50. Miao, H. et al. Observation of double Weyl phonons in parity-breaking FeSi. *Phys. Rev. Lett.* **121**, 035302 (2018).
51. Young, S. M. et al. Dirac semimetal in three dimensions. *Phys. Rev. Lett.* **108**, 140405 (2012).
52. Wang, Z. et al. Dirac semimetal and topological phase transitions in A_3Bi (A=Na, K, Rb). *Phys. Rev. B* **85**, 195320 (2012).
53. Liu, Z. K. et al. Discovery of a three-dimensional topological Dirac semimetal, Na_3Bi. *Science* **343**, 864–867 (2014).
54. Xu, S.-Y. et al. Observation of Fermi arc surface states in a topological metal. *Science* **347**, 294–298 (2015).
55. Wieder, B. J. et al. Double Dirac semimetals in three dimensions. *Phys. Rev. Lett.* **116**, 186402 (2016).
56. Burkov, A. A., Hook, M. D. & Balents, L. Topological nodal semimetals. *Phys. Rev. B* **84**, 235126 (2011).
57. Phillips, M. & Aji, V. Tunable line node semimetals. *Phys. Rev. B* **90**, 115111 (2014).
58. Chiu, C. K. & Schnyder, A. P. Classification of reflection-symmetry-protected topological semimetals and nodal superconductors. *Phy. Rev. B* **90**, 205136 (2014).
59. Fang, C., Chen, Y., Kee, H. Y. & Fu, L. Topological nodal line semimetals with and without spin-orbital coupling. *Phys. Rev. B* **92**, 081201 (2015).
60. Kim, Y., Wieder, B. J., Kane, C. L. & Rappe, A. M. Dirac line nodes in inversion-symmetric crystals. *Phys. Rev. Lett.* **115**, 036806 (2015).
61. Yu, R., Weng, H., Fang, Z., Dai, X. & Hu, X. Topological node-line semimetal and Dirac semimetal state in antiperovskite Cu_3PdN. *Phys. Rev. Lett.* **115**, 036807 (2015).
62. Xie, L. S. et al. A new form of Ca_3P_2 with a ring of Dirac nodes. *APL Mater.* **3**, 083602 (2015).
63. Bian, G. et al. Drumhead surface states and topological nodal-line fermions in $TlTaSe_2$. *Phys. Rev. B* **93**, 121113 (2016).
64. Bian, G. et al. Topological nodal-line fermions in spin-orbit metal $PbTaSe_2$. *Nat. Commun.* **7**, 10556 (2016).
65. Schoop, L. M. et al. Dirac cone protected by non-symmorphic symmetry and three-dimensional Dirac line node in ZrSiS. *Nat. Commun.* **7**, 11696 (2016).
66. Neupane, M. et al. Observation of topological nodal fermion semimetal phase in ZrSiS. *Phys. Rev. B* **93**, 201104(R) (2016).
67. Hu, J. et al. Evidence of topological nodal-line fermions in ZrSiSe and ZrSiTe. *Phys. Rev. Lett.* **117**, 016602 (2016).
68. Hosen, M. M. et al. Tunability of the topological nodal-line semimetal phase in ZrSiX-type materials (X=S, Se, Te). *Phys. Rev. B* **95**, 161101(R) (2017).
69. Zhu, Z. et al. Quasiparticle interference and nonsymmorphic effect on a floating band surface state of ZrSiSe. *Nat. Commun.* **9**, 4153 (2018).
70. Bzdušek, T. et al. Nodal-chain metals. *Nature* **538**, 75–78 (2016).
71. Chang, G. et al. Topological Hopf and chain link semimetal states and their application to Co_2MnGa. *Phys. Rev. Lett.* **119**, 156401 (2017).
72. Chen, W., Lu, H. Z. & Hu, J.-M. Topological semimetals with a double-helix nodal link. *Phys. Rev. B* **96**, 041102(R) (2017).
73. Yan, Z. et al. Nodal-link semimetals. *Phys. Rev. B* **96**, 041103(R) (2017).
74. Chang, P.-Y. & Yee, C.-H. Weyl-link semimetals. *Phys. Rev. B* **96**, 081114(R) (2017).
75. Ezawa, M. Topological semimetals carrying arbitrary Hopf numbers: Fermi surface topologies of a Hopf link, Solomon's knot, trefoil knot, and other linked nodal varieties. *Phys. Rev. B* **96**, 041202(R) (2017).
76. Bi, R., Yan, Z., Lu, L. & Wang, Z. Nodal-knot semimetals. *Phys. Rev. B* **96**, 201305(R) (2017).
77. Belopolski, I. et al. Discovery of topological Weyl lines and drumhead surface states in a room-temperature magnet. *Science* **365**, 1278–1281 (2019).
78. Weng, H. et al. Topological semimetals with triply degenerate nodal points in θ-phase tantalum nitride. *Phys. Rev. B* **93**, 241202 (2016).
79. Zhu, Z. et al. Triple point topological metals. *Phys. Rev. X* **6**, 031003 (2016).
80. Chang, G. et al. Nexus fermions in topological symmorphic crystalline metals. *Sci. Rep.* **7**, 1688 (2017).
81. Georg, W. W. et al. Topological phases in $InAs_{1-x}Sb_x$: from novel topological semimetal to Majorana wire. *Phys. Rev. Lett.* **117**, 076403 (2016).
82. Lv, B. Q. et al. Observation of three-component fermions in the topological semimetal molybdenum phosphide. *Nature* **546**, 627–631 (2017).
83. Ma, J.-Z. et al. Three-component fermions with surface Fermi arcs in tungsten carbide. *Nat. Phys.* **14**, 349–354 (2018).
84. Meng, T. & Balents, L. Weyl superconductors. *Phys. Rev. B* **86**, 1054504 (2012).
85. Bardarson, J. H., Lu, Y.-M. & Moore, J. E. Superconductivity of doped Weyl semimetals: finite-momentum pairing and electronic analogues of the ^{3}He-A phase. *Phys. Rev. B* **86**, 214514 (2012).
86. Hosur, P. & Qi, X.-L. Time-reversal invariant topological superconductivity in doped Weyl semimetals. *Phys. Rev. B* **90**, 045130 (2014).
87. Bednik, G., Zyuzin, A. A. & Burkov, A. A. Superconductivity in Weyl semimetals. *Phys. Rev. B* **92**, 035153 (2015).
88. Li, Y. & Haldane, F. D. M. Topological nodal Cooper pairing in doped Weyl seimetals. *Phys. Rev. Lett.* **120**, 067003 (2018).
89. Burkov, A. A. Anomalous Hall effect in Weyl metals. *Phys. Rev. Lett.* **113**, 187202 (2014).
90. Duval, C., Horvath, Z., Horvathy, P. A., Martina, L. & Stichel, P. C. Berry phase correction to electron density in solids and "exotic" dynamics. *Mod. Phys. Lett. B* **20**, 373–378 (2006).
91. Son, D. T. & Spivak, B. Z. Chiral anomaly and classical negative magnetoresistance of Weyl metals. *Phys. Rev. B* **88**, 104412 (2013).
92. Burkov, A. A. Chiral anomaly and diffusive magnetotransport in Weyl metals. *Phys. Rev. Lett.* **113**, 247203 (2014).
93. Xiong, J. et al. Evidence for the chiral anomaly in the Dirac semimetal Na_3Bi. *Science* **350**, 413–416 (2015).
94. Fukushima, K., Kharzeev, D. E. & Warringa, H. J. Chiral magnetic effect. *Phys. Rev. D.* **78**, 074033 (2008).
95. Zyuzin, A. A., Wu, S. & Burkov, A. A. Weyl semimetal with broken time reversal and inversion symmetries. *Phys. Rev. B* **85**, 165110 (2012).
96. Ma, K. & Pesin, D. A. Chiral magnetic effect and natural optical activity in metals with or without Weyl points. *Phys. Rev. B* **92**, 235205 (2015).
97. Sodemann, I. & Fu, L. Quantum nonlinear Hall effect induced by Berry curvature dipole in time-reversal invariant materials. *Phys. Rev. Lett.* **115**, 216806 (2015).
98. Parameswaran, S. A., Grover, T., Abanin, D. A., Pesin, D. A. & Vishwanath, A. Probing the chiral anomaly with nonlocal transport in three-dimensional topological semimetals. *Phys. Rev. X* **4**, 031035 (2014).

99. Baum, Y. Current at a distance and resonant transparency in Weyl semimetals. *Phys. Rev. X* **5**, 041046 (2015).
100. Hosur, P. Friedel oscillations due to Fermi arcs in Weyl semimetals. *Phys. Rev. B* **86**, 195102 (2012).
101. Potter, A. C., Kimchi, I. & Vishwanath, A. Quantum oscillations from surface Fermi arcs in Weyl and Dirac semimetals. *Nat. Commun.* **5**, 5161 (2014).
102. Zhang, C. et al. Evolution of Weyl orbit and quantum Hall effect in Dirac semimetal Cd_3As_2. *Nat. Commun.* **8**, 1272 (2017).
103. Zhang, C. et al. Quantum Hall effect based on Weyl orbits in Cd_3As_2. *Nature* **565**, 331–336 (2019).
104. Ishizuka, H., Hayata, T., Ueda, M. & Nagaosa, N. Emergent electromagnetic induction and adiabatic charge pumping in Weyl semimetals. *Phys. Rev. Lett.* **117**, 216601 (2016).
105. Morimoto, T., Zhong, S., Orenstein, J. & Moore, J. E. Semiclassical theory of nonlinear magneto-optical responses with applications to topological Dirac/Weyl semimetals. *Phys. Rev. B* **94**, 245121 (2016).
106. Chan, C.-K., Lindner, N. H., Refael, G. & Lee, P. A. Photocurrents in Weyl semimetals. *Phys. Rev. B* **95**, 041104 (2017).
107. de Juan, F., Grushin, A. G., Morimoto, T. & Moore, J. E. Quantized circular photogalvanic effect in Weyl semimetals. *Nat. Commun.* **8**, 15995 (2017).
108. Wu, L. et al. Giant anisotropic nonlinear optical response in transition metal monopnictide Weyl semimetals. *Nat. Phys.* **13**, 350–355 (2016).
109. Ma, Q. et al. Direct optical detection of Weyl fermion chirality in a topological semimetal. *Nat. Phys.* **13**, 842–847 (2017).
110. Osterhoudt, G. B. et al. Colossal mid-infrared bulk photovoltaic effect in a type-I Weyl semimetal. *Nat. Mater.* **18**, 471–475 (2019).
111. Ma, J. et al. Nonlinear photoresponse of type-II Weyl semimetals. *Nat. Mater.* **18**, 476–481 (2019).
112. Rees, D. et al. Helicity-dependent photocurrents in the chiral Weyl semimetal RhSi. *Sci. Adv.* **6**, eaba0509 (2020).
113. Chang, G. et al. Unconventional photocurrents from surface Fermi arcs in topological chiral semimetals. *Phys. Rev. Lett.* **124**, 166404 (2020).
114. Xu, S.-Y. et al. Discovery of a Weyl fermion state with Fermi arcs in niobium arsenide. *Nat. Phys.* **11**, 748–754 (2015).
115. Lv, B. Q. et al. Observation of Weyl nodes in TaAs. *Nat. Phys.* **11**, 724–727 (2015).
116. Yang, L. et al. Weyl semimetal phase in the non-centrosymmetric compound TaAs. *Nat. Phys.* **11**, 728–732 (2015).
117. Xu, S.-Y. et al. Experimental discovery of a topological Weyl semimetal state in TaP. *Sci. Adv.* **1**, e1501092 (2015).
118. Xu, N. et al. Observation of Weyl nodes and Fermi arcs in tantalum phosphide. *Nat. Commun.* **7**, 11006 (2016).
119. Belopolski, I. et al. Criteria for directly detecting topological Fermi arcs in Weyl semimetals. *Phys. Rev. Lett.* **116**, 066802 (2016).
120. Liu, Z. K. et al. Evolution of the Fermi surface of Weyl semimetals in the transition metal pnictide family. *Nat. Mater.* **15**, 27–31 (2016).
121. Lv, B. Q. et al. Observation of Fermi-arc spin texture in TaAs. *Phys. Rev. Lett.* **115**, 217601 (2016).
122. Xu, S.-Y. et al. Spin polarization and texture of the Fermi arcs in the Weyl fermion semimetal TaAs. *Phys. Rev. Lett.* **116**, 096801 (2016).
123. Zheng, H. et al. Atomic-scale visualization of quantum interference on a Weyl semimetal surface by scanning tunneling microscopy. *ACS Nano* **10**, 1378–1385 (2016).
124. Inoue, H. et al. Quasiparticle interference of the Fermi arcs and surface-bulk connectivity of a Weyl semimetal. *Science* **351**, 1184–1187 (2016).
125. Batabyal, R. et al. Visualizing weakly bound surface Fermi arcs and their correspondence to bulk Weyl fermions. *Sci. Adv.* **2**, e1600709 (2016).
126. Huang, X. et al. Observation of the chiral-anomaly-induced negative magnetoresistance in 3D Weyl semimetal TaAs. *Phys. Rev. X* **5**, 031023 (2015).
127. Zhang, C. et al. Observation of the Adler-Bell-Jackiw chiral anomaly in a Weyl semimetal. *Nat. Commun.* **7**, 10735 (2016).
128. Ghimire, N. J. et al. Magnetotransport of single crystalline NbAs. *J. Phys. Condens. Matter* **27**, 152201 (2015).
129. Arnold, F. et al. Negative magnetoresistance without well-defined chirality in the Weyl semimetal TaP. *Nat. Commun.* **7**, 11615 (2016).
130. Zhang, C. et al. Magnetic-tunnelling-induced Weyl node annihilation in TaP. *Nat. Phys.* **13**, 979–986 (2017).
131. Shekhar, C. et al. Extremely large magnetoresistance and ultrahigh mobility in the topological Weyl semimetal candidate NbP. *Nat. Phys.* **11**, 645–649 (2015).
132. Zhang, C. et al. Large magnetoresistance over an extended temperature regime in monophosphides of tantalum and niobium. *Phys. Rev. B* **92**, 041203(R) (2015).
133. Luo, Y. et al. Electron-hole compensation effect between topologically trivial electrons and nontrivial holes in NbAs. *Phys. Rev. B* **92**, 205134 (2015).
134. Sun, Y., Wu, S.-C., Ali, M. N., Felser, C. & Yan, B. Prediction of the Weyl semimetal in orthorhombic $MoTe_2$. *Phys. Rev. B* **92**, 161107(R) (2015).
135. Chang, T.-R. et al. Arc-tunable Weyl fermion metallic state in $Mo_xW_{1-x}Te_2$. *Nat. Commun.* **7**, 10639 (2016).
136. Wang, Z. et al. $MoTe_2$: A type-II Weyl topological metal. *Phys. Rev. Lett.* **117**, 056805 (2016).
137. Huang, L. et al. Spectroscopic evidence for type II Weyl semimetal state in $MoTe_2$. *Nat. Mater.* **15**, 1155–1160 (2016).
138. Deng, K. et al. Experimental observation of topological Fermi arcs in type-II Weyl semimetal $MoTe_2$. *Nat. Phys.* **12**, 1105–1110 (2016).
139. Belopolski, I. et al. Discovery of a new type of topological Weyl fermion semimetal state in $Mo_xW_{1-x}Te_2$. *Nat. Commun.* **7**, 13643 (2016).
140. Belopolski, I. et al. Fermi arc electronic structure and Chern numbers in the type-II Weyl semimetal candidate $Mo_xW_{1-x}Te_2$. *Phys. Rev. B* **94**, 085127 (2016).
141. Bruno, F. Y. et al. Observation of large topologically trivial Fermi arcs in the candidate type-II Weyl semimetal WTe_2. *Phys. Rev. B* **94**, 121112(R) (2016).
142. Tamai, A. et al. Fermi arcs and their topological character in the candidate type-II Weyl semimetal $MoTe_2$. *Phys. Rev. X* **6**, 031021 (2016).
143. Jiang, J. et al. Signature of type-II Weyl semimetal phase in $MoTe_2$. *Nat. Commun.* **8**, 13973 (2017).
144. Zheng, H. et al. Atomic-scale visualization of quasiparticle interference on a type-II Weyl semimetal surface. *Phys. Rev. Lett.* **117**, 266804 (2017).
145. Iaia, D. et al. Searching for topological Fermi arcs via quasiparticle interference on a type-II Weyl semimetal $MoTe_2$. *npj Quantum Mater.* **3**, 38 (2018).
146. Xu, S.-Y. et al. Discovery of Lorentz-violating type II Weyl fermions in LaAlGe. *Sci. Adv.* **3**, e1603266 (2017).
147. Ali, M. N. et al. Large, non-saturating magnetoresistance in WTe_2. *Nature* **514**, 205–208 (2014).
148. Pletikosić, I. et al. Electronic structure basis for the extraordinary magnetoresistance in WTe_2. *Phys. Rev. Lett.* **113**, 216601 (2014).
149. Qian, X., Liu, J., Fu, L. & Li, J. Quantum spin Hall effect in two-dimensional transition metal dichalcogenides. *Science* **346**, 1344–1347 (2014).
150. Fei, Z. et al. Edge conduction in monolayer WTe_2. *Nat. Phys.* **13**, 677–682 (2017).
151. Tang, S. et al. Quantum spin Hall state in monolayer 1T′-WTe_2. *Nat. Phys.* **13**, 683–687 (2017).
152. Wu, S. et al. Observation of the quantum spin Hall effect up to 100 kelvin in a monolayer crystal. *Science* **359**, 76–79 (2017).
153. Chang, G. et al. Magnetic and noncentrosymmetric Weyl fermion semimetal states in the RAlGe family of compounds (R=rare earth). *Phys. Rev. B* **97**, 041104(R) (2018).
154. Suzuki, T. et al. Singular angular magnetoresistance in a magnetic nodal semimetal. *Science* **365**, 377–381 (2019).
155. Fang, C., Lu, L., Liu, J. & Fu, L. Topological semimetals with helicoid surface states. *Nat. Phys.* **12**, 936–941 (2016).
156. Yang, B. et al. Ideal Weyl points and helicoid surface states in artificial photonic crystal structures. *Science* **359**, 1013–1016 (2018).
157. Fang, C. et al. Multi-Weyl topological semimetals stabilized by point group symmetry. *Phys. Rev. Lett.* **108**, 266802 (2012).
158. Xu, G. et al. Chern semi-metal and quantized anomalous Hall effect in $HgCr_2Se_4$. *Phys. Rev. Lett.* **107**, 186806 (2011).
159. Huang, S.-M. et al. New type of Weyl semimetal with quadratic double Weyl fermions. *Proc. Natl Acad. Sci. USA* **113**, 1180–1185 (2016).
160. Shapiro, M. C. et al. Structure and magnetic properties of the pyrochlore iridate $Y_2Ir_2O_7$. *Phys. Rev. B* **85**, 214434 (2012).
161. Liu, H. et al. Magnetic order, spin dynamics and transport properties of the pyrochlore iridate $Y_2Ir_2O_7$. *Solid State Commun.* **179**, 1–5 (2012).
162. Belopolski, I. et al. A novel artificial condensed matter lattice and a new platform for one-dimensional topological phases. *Sci. Adv.* **3**, e1501692 (2017).
163. Guan, T. et al. Evidence for half-metallicity in *n*-type $HgCr_2Se_4$. *Phys. Rev. Lett.* **115**, 087002 (2015).
164. Adler, S. Axial-vector vertex in spinor electrodynamics. *Phys. Rev.* **177**, 2426–2438 (1969).
165. Bell, J. S. & Jackiw, R. A PCAC puzzle: $\pi^0 \rightarrow \gamma\gamma$ in the σ-model. *Nuovo Cim. A* **60**, 47–61 (1969).
166. dos Reis, R. D. et al. On the search for the chiral anomaly in Weyl semimetals: the negative longitudinal magnetoresistance. *New J. Phys.* **18**, 085006 (2016).
167. Dai, X., Du, Z. Z. & Lu, H.-Z. Negative magnetoresistance without chiral anomaly in topological insulators. *Phys. Rev. Lett.* **119**, 166601 (2017).
168. Andreev, A. V. & Spivak, B. Z. Longitudinal negative magnetoresistance and magnetotransport phenomena in conventional and topological conductors. *Phys. Rev. Lett.* **120**, 026601 (2018).
169. Wang, Z. et al. Three-dimensional Dirac semimetal and quantum transport in Cd_3As_2. *Phys. Rev. B* **88**, 125427 (2013).
170. Liang, T. et al. Ultrahigh mobility and giant magnetoresistance in the Dirac semimetal Cd_3As_2. *Nat. Mater.* **14**, 280–284 (2014).
171. Razzoli, E. et al. Stable Weyl points, trivial surface states and particle-hole compensation in WP_2. *Phys. Rev. B* **97**, 201103 (2018).
172. Sanchez, D. S. et al. Observation of Weyl fermions in a magnetic non-centrosymmetric crystal. *Nat. Commun.* **11**, 3356 (2020).
173. Flicker, F. et al. Chiral optical response of multifold fermions. *Phys. Rev. B* **98**, 155145 (2018).
174. Zhuoliang, N. et al. Giant topological longitudinal circular photo-galvanic effect in the chiral multifold semimetal CoSi. *Nat. Commun.* **12**, 154 (2021).
175. Schröter, N. B. M. et al. Observation and control of maximal Chern numbers in a chiral topological semimetal. *Science* **369**, 179–183 (2020).
176. Cochran, T. A. et al. A Fermi arc quantum ladder. Preprint at *arXiv* 2004.11365 (2020).
177. Yan, Q. et al. Experimental discovery of nodal chains. *Nat. Phys.* **14**, 461–464 (2018).
178. Neto, E. H. & da, S. "Weyl"ing away time-reversal symmetry. *Science* **365**, 1248–1249 (2019).
179. Sakai, A. et al. Giant anomalous Nernst effect and quantum-critical scaling in a ferromagnetic semimetal. *Nat. Phys.* **14**, 1119–1124 (2018).
180. Reichlova, H. et al. Large anomalous Nernst effect in thin films of the Weyl semimetal Co_2MnGa. *Appl. Phys. Lett.* **113**, 212405 (2018).
181. Manna, K. et al. From colossal to zero: controlling the anomalous Hall effect in magnetic Heusler compounds via Berry curvature design. *Phys. Rev. X* **8**, 041045 (2018).
182. Sakai, A. et al. Iron-based binary ferromagnets for transverse thermoelectric conversion. *Nature* **581**, 53–57 (2020).
183. Kim, K. et al. Large anomalous Hall current induced by topological nodal lines in a ferromagnetic van der Waals semimetal. *Nat. Mater.* **17**, 794–799 (2018).
184. Liu, E. et al. Giant anomalous Hall effect in a ferromagnetic kagome-lattice semimetal. *Nat. Phys.* **14**, 1125–1131 (2018).
185. Wang, Q. et al. Large intrinsic anomalous Hall effect in half-metallic ferromagnet $Co_3Sn_2S_2$ with magnetic Weyl fermions. *Nat. Commun.* **9**, 3681 (2018).
186. Xu, Q. et al. Topological surface Fermi arcs in the magnetic Weyl semimetal $Co_3Sn_2S_2$ with magnetic Weyl fermions. *Phys. Rev. B* **97**, 235416 (2018).
187. Liu, D. F. et al. Magnetic Weyl semimetal phase in a Kagomé crystal. *Science* **365**, 1282–1285 (2019).
188. Morali, N. et al. Fermi-arc diversity on surface terminations of the magnetic Weyl semimetal $Co_3Sn_2S_2$. *Science* **365**, 1286–1291 (2019).
189. Guin, S. N. et al. Zero-field Nernst effect in a ferromagnetic kagome-lattice Weyl-semimetal $Co_3Sn_2S_2$. *Adv. Mat.* **31**, 1806622 (2019).
190. Zhou, H. et al. Enhanced anomalous Hall effect in the magnetic topological semimetal $Co_3Sn_{2-x}In_xS_2$. *Phys. Rev. B* **101**, 125121 (2020).
191. Belopolski, I. et al. Signatures of a topological Weyl loop in $Co_3Sn_2S_2$. Preprint at *arXiv* 2005.02400 (2020).
192. Ye, L. et al. Massive Dirac fermions in a ferromagnetic kagome metal. *Nature* **555**, 638–642 (2018).

193. Yin, J.-X. et al. Giant and anisotropic many-body spin–orbit tunability in a strongly correlated kagome magnet. *Nature* **562**, 91–95 (2018).
194. Nakatsuji, S., Kiyohara, N. & Higo, T. Large anomalous Hall effect in a non-collinear antiferromagnet at room temperature. *Nature* **527**, 212–215 (2015).
195. Ikhlas, M. et al. Large anomalous Nernst effect at room temperature in a chiral antiferromagnet. *Nat. Phys.* **13**, 1085–1090 (2017).
196. Kuroda, K. et al. Evidence for magnetic Weyl fermions in a correlated metal. *Nat. Mater.* **16**, 1090–1095 (2017).
197. Yang, H. et al. Topological Weyl semimetals in the chiral antiferromagnetic materials Mn_3Ge and Mn_3Sn. *New J. Phys.* **19**, 015008 (2017).
198. Zhang, T. et al. Catalogue of topological electronic materials. *Nature* **566**, 475–479 (2019).
199. Vergniory, M. G. et al. A complete catalogue of high-quality topological materials. *Nature* **566**, 480–485 (2019).
200. Tang, F., Po, H. C., Vishwanath, A. & Wan, X. Comprehensive search for topological materials using symmetry indicators. *Nature* **566**, 486–489 (2019).
201. Zunger, A. Beware of plausible predictions of fantasy materials. *Nature* **566**, 447–449 (2019).
202. Xiao, D., Chang, M. C. & Niu, Q. Berry phase effects on electronic properties. *Rev. Mod. Phys.* **82**, 1959–2007 (2010).
203. Resta, R. Electrical polarization and orbital magnetization: the modern theories. *J. Phys. Condens. Matter* **22**, 123201 (2010).
204. Yin, J.-X. et al. Negative flat band magnetism in a spin–orbit-coupled correlated kagome magnet. *Nat. Phys.* **15**, 443–448 (2019).
205. Yin, J. -X. et al. Quantum-limit Chern topological magnetism in $TbMn_6Sn_6$. *Nature* **583**, 533–536 (2020).
206. Yin, J. -X. et al. Fermion–boson many-body interplay in a frustrated kagome paramagnet. *Nat. Commun.* **11**, 4003 (2020).
207. Zhang, S.S. et al. Many-body resonance in a correlated topological kagome antiferromagnet. *Phys. Rev. Lett.* **125**, 046401 (2020).
208. He, K., Wang, Y. & Xue, Q.-K. Topological materials: quantum anomalous Hall system. *Annu. Rev. Condens. Matter Phys.* **9**, 329–344 (2018).
209. Yin, J.-X., Pan, S. H. and Hasan, M. Z. Probing topological quantum matter with scanning tunnelling microscopy. *Nat. Rev. Phys.* https://doi.org/10.1038/s42254-021-00293-7 (2021).
210. Wang, Y. et al. Gate-tunable negative longitudinal magnetoresistance in the predicted type-II Weyl semimetal WTe_2. *Nat. Commun.* **7**, 13142 (2016).
211. Koepernik, K. et al. $TaIrTe_4$ a ternary type-II Weyl semimetal. *Phys. Rev. B* **93**, 201101(R) (2016).
212. Belopolski, I. et al. Signatures of a time-reversal symmetric Weyl semimetal with only four Weyl points. *Nat. Commun.* **8**, 942 (2017).
213. Haubold, E. et al. Experimental realization of type-II Weyl state in non-centrosymmetric $TaIrTe_4$. *Phys. Rev. B* **95**, 241108(R) (2017).
214. Kim, S. et al. Magnetotransport and de Haas–van Alphen measurements in the type-II Weyl semimetal $TaIrTe_4$. *Phys. Rev. B* **94**, 165145 (2016).
215. Autés, G. et al. Robust type-II Weyl semimetal phase in transition metal diphosphides XP_2 (X = Mo, W). *Phys. Rev. Lett.* **117**, 066402 (2016).
216. Kumar, N. et al. Extremely high magnetoresistance and conductivity in the type-II Weyl semimetals WP_2 and MoP_2. *Nat. Commun.* **8**, 1642 (2017).
217. Singh, B. et al. Topological electronic structure and Weyl semimetal in the $TlBiSe_2$ class of semiconductors. *Phys. Rev. B* **86**, 115208 (2012).
218. Halász, G. B. & Balents, L. Time-reversal invariant realization of the Weyl semimetal phase. *Phys. Rev. B* **85**, 035103 (2012).
219. Liu, J. & Vanderbilt, D. Weyl semimetals from noncentrosymmetric topological insulators. *Phys. Rev. B* **90**, 155316 (2014).
220. Hirayama, M., Okugawa, R., Ishibashi, S., Murakami, S. & Miyake, T. Weyl node and spin texture in trigonal tellurium and selenium. *Phys. Rev. Lett.* **114**, 206401 (2015).
221. Chang, G. et al. A strongly robust Weyl fermion semimetal state in Ta_3S_2. *Sci. Adv.* **2**, e1600295 (2016).
222. Chen, D. et al. Magnetotransport properties of the type II Weyl semimetal candidate Ta_3S_2. *Phys. Rev. B* **94**, 174411 (2016).
223. Ruan, J. et al. Ideal Weyl semimetals in the chalcopyrites $CuTlSe_2$, $AgTlTe_2$, $AuTlTe_2$ and $ZnPbAs_2$. *Phys. Rev. Lett.* **116**, 226801 (2016).
224. Liu, C.-C., Zhou, J.-J., Yao, Y. & Zhang, F. Weak topological insulators and composite Weyl semimetals: β-Bi_4X_4 (X=Br, I). *Phys. Rev. Lett.* **116**, 066801 (2016).
225. Zhang, C.-L. et al. Ultraquantum magnetoresistance in the Kramers-Weyl semimetal candidate β-Ag_2Se. *Phys. Rev. B* **96**, 165148 (2017).
226. Kim, H.-J. et al. Dirac versus Weyl fermions in topological insulators: Adler-Bell-Jackiw anomaly in transport phenomena. *Phys. Rev. Lett.* **111**, 246603 (2013).
227. Bulmash, D., Liu, C.-X. & Qi, X.-L. Prediction of a Weyl semimetal in $Hg_{1-x-y}Cd_xMn_yTe$. *Phys. Rev. B* **89**, 081106(R) (2014).
228. Borisenko, S. et al. Time-reversal symmetry breaking Weyl state in $YbMnBi_2$. *Nat. Commun.* **10**, 3424 (2019).
229. Schoop, L. M. et al. Tunable Weyl and Dirac states in the nonsymmorphic compound CeSbTe. *Sci. Adv.* **4**, eaar2317 (2018).
230. Hirschberger, M. et al. The chiral anomaly and thermopower of Weyl fermions in the half-Heusler GdPtBi. *Nat. Mater.* **15**, 1161–1165 (2016).
231. Wang, Z. et al. Time-reversal-breaking Weyl fermions in magnetic Heusler alloys. *Phys. Rev. Lett.* **117**, 236401 (2016).
232. Chang, G. et al. Room-temperature magnetic topological Weyl fermion and nodal line semimetal states in half-metallic Heusler Co_2TiX (X=Si, Ge, or Sn). *Sci. Rep.* **6**, 38839 (2016).
233. Fischer, M. F. et al. Chiral *d*-wave superconductivity in SrPtAs. *Phys. Rev. B* **89**, 020509(R) (2014).
234. Biswas, P. K. et al. Evidence for superconductivity with broken time-reversal symmetry in locally non-centrosymmetric SrPtAs. *Phys. Rev. B* **87**, 180503(R) (2013).
235. Goswami, P. & Balicas, L. Topological properties of possible Weyl superconducting states of URu_2Si_2. Preprint at *arXiv* 1312.3632 (2013).
236. Goswami, P. & Nevidomskyy, A. H. Topological Weyl superconductor to diffusive thermal Hall metal crossover in the B phase of UPt_3. *Phys. Rev. B* **92**, 214504 (2015).

Acknowledgements

We acknowledge P. W. Anderson, D. A. Huse, F. D. M. Haldane, N. P. Ong and E. Lieb for discussions on quantum magnets, topological matter, spin liquids and superconductivity. We further acknowledge insightful discussions with Alexei V. Federov, Arun Bansil, BaoKai Wang, Benjamin J Wieder, Biao Lian, Chang Liu, Chenglong Zhang, Chi-Cheng Lee, Ching-Kai Chiu, Claudia Felser, Daniel Multer, Daniel S. Sanchez, David Hsieh, Dong Qian, Donghui Lu, Fangcheng Chou, Hao Zheng, Hechang Lei, Horng-Tay Jeng, Hsin Lin, Huibin Zhou, Jie Ma, Jonathan Denlinger, Kaustuv Manna, L. Andrew Wray, Madhab Neupane, Makoto Hashimoto, Maksim Litskevich, Md Shafayat Hossain, Nana Shumiya, Nasser Alidoust, Niels B. M. Schröter, Pavel P. Shibayev, Qi Zhang, Raman Sankar, Shik Shin, Shin-Ming Huang, Shuang Jia, Songtian S. Zhang, Stepan S Tsirkin, Sung-Kwan Mo, Takeshi Kondo, Tay-Rong Chang, Titus Neupert, Tyler A. Cochran, Weiwei Xie, Vicky Süß, Vladimir N. Strocov, Xian P Yang, Yukiaki Ishida, Yuqi Xia, Yuxiao Jiang, Zahid Hussain, Zheng Liu, Zhujun Yuan, Zi-Jia Cheng and Zurab Guguchia. We acknowledge experimental collaboration with Vladimir N. Strocov, Niels B. M. Schröter and Alla Chikina (ADRESS endstation, Swiss Light Source, Paul Scherrer Institut, Proposal #20180896) in acquiring data presented in Fig. 5c, the details of which will be published in a forthcoming article. Spectroscopy work led by Princeton University was supported by the United States Department of Energy (U.S. DOE) under the Basic Energy Sciences programme (grant number DOE/BES DE-FG-02-05ER46200; M.Z.H.). The theoretical work and sample characterization are supported by the Gordon and Betty Moore Foundation (GBMF4547 and GBMF9461; M.Z.H.). The sample characterization related to topological magnetism and superconductivity is partly based on support by the U.S. DOE, Office of Science through the Quantum Science Center (QSC), a National Quantum Information Science Research Center at the Oak Ridge National Laboratory. G.C. would like to acknowledge the support of the National Research Foundation, Singapore under its NRF Fellowship Award (NRF-NRFF13-2021-0010) and the Nanyang Assistant Professorship grant from Nanyang Technological University. S.Y.X. was supported by the Center for the Advancement of Topological Semimetals, an Energy Frontier Research Center funded by the U.S. Department of Energy (DOE) Office of Science, through the Ames Laboratory under contract DE-AC0207CH11358. S.Y.X. acknowledges the Corning Fund for Faculty Development. G.B. was supported by the US National Science Foundation under Grant No. NSF DMR-1809160.

Author contributions

The authors contributed equally to all aspects of the article.

Competing interests

The authors declare no competing interests.

Publisher's note

Springer Nature remains neutral with regard to jurisdictional claims in published maps and institutional affiliations.